

## Gas tungsten arc welding of as-cast AlCoCrFeNi<sub>2.1</sub> eutectic high entropy alloy



Jiajia Shen<sup>a</sup>, Priyanka Agrawal<sup>b,c</sup>, Tiago A. Rodrigues<sup>a</sup>, J.G. Lopes<sup>a</sup>, N. Schell<sup>d</sup>, Zhi Zeng<sup>e</sup>, Rajiv S. Mishra<sup>b,c</sup>, J.P. Oliveira<sup>a,f,\*</sup>

<sup>a</sup> UNIDEMI, Department of Mechanical and Industrial Engineering, NOVA School of Science and Technology, Universidade NOVA de Lisboa, Caparica 2829-516, Portugal

<sup>b</sup> Center for Friction Stir Processing, Department of Materials Science and Engineering, University of North Texas, Denton, TX 76207, USA

<sup>c</sup> Advanced Materials and Manufacturing Processes Institute, University of North Texas, Denton, TX 76207, USA

<sup>d</sup> Institute of Materials Physics, Helmholtz-Zentrum Hereon, Max-Planck-Str. 1, Geesthacht D-21502, Germany

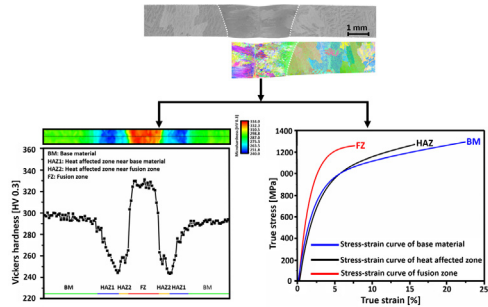
<sup>e</sup> School of Mechanical and Electrical Engineering, University of Electronic Science and Technology of China, Sichuan 611731, China

<sup>f</sup> CENIMAT/I3N, Department of Materials Science, NOVA School of Science and Technology, Universidade NOVA de Lisboa, 2829-516 Caparica, Portugal

### HIGHLIGHTS

- Gas tungsten arc welding was used to join an as-cast AlCoCrFeNi<sub>2.1</sub> eutectic high entropy alloy.
- No welding defects were observed.
- Synchrotron X-ray diffraction, electron microscopy and thermodynamic calculations used to evaluate the joint microstructure.
- The fusion zone exhibits the highest hardness due to a refined interlamellar thickness.
- The welded joints present a good strength/ductility balance.

### GRAPHICAL ABSTRACT



### ARTICLE INFO

#### Article history:

Received 9 June 2022

Revised 31 August 2022

Accepted 18 September 2022

Available online 20 September 2022

#### Keywords:

Eutectic high entropy alloys

AlCoCrFeNi<sub>2.1</sub>

Gas tungsten arc welding

Synchrotron X-ray diffraction

Thermodynamic calculations

Mechanical testing

Digital image correlation

### ABSTRACT

The AlCoCrFeNi<sub>2.1</sub> eutectic high entropy alloy is of great interest due to its unique mechanical properties combining both high strength and plasticity. Here, gas tungsten arc welding was performed for the first time on an as-cast AlCoCrFeNi<sub>2.1</sub> alloy. The microstructural evolution of the welded joints was assessed by combining electron microscopy with electron backscatter diffraction, synchrotron X-ray diffraction analysis and thermodynamic calculations. Microhardness mapping and tensile testing coupled with digital image correlation were used to investigate the strength distribution across the joint. The base material, heat affected zone and fusion zone are composed of an FCC + B2 BCC eutectic structure, although the relative volume fractions vary across the joint owing to the weld thermal cycle. The BCC nanoprecipitates that existed in the base material started to dissolve into the matrix in the heat affected zone and closer to the fusion zone boundary. Compared to the as-cast base material, the fusion zone evidenced grain refinement owing to the higher cooling rate experienced during solidification. This translates into an increased hardness in this region. The joints exhibit good strength/ductility balance with failure occurring in the base material. This work establishes the potential for using arc-based welding for joining eutectic high entropy alloys.

© 2022 The Authors. Published by Elsevier Ltd. This is an open access article under the CC BY license (<http://creativecommons.org/licenses/by/4.0/>).

\* Corresponding author at: CENIMAT/I3N, Department of Materials Science, NOVA School of Science and Technology, Universidade NOVA de Lisboa, 2829-516 Caparica, Portugal.

E-mail addresses: [j.shen@campus.fct.unl.pt](mailto:j.shen@campus.fct.unl.pt) (J. Shen), [jp.oliveira@fct.unl.pt](mailto:jp.oliveira@fct.unl.pt) (J.P. Oliveira).

## 1. Introduction

High entropy alloys were first discovered independently by Yeh et al. [1] and Cantor et al. [2] in 2004. Their revolutionary design concept escaped from typical engineering alloys with only one or two principal elements and used at least five principal elements, each with an atomic content varying between 5 and 35 at. %. Four “core effects” are commonly attributed to high entropy alloys: the high entropy effect [1], the lattice distortion effect [3], the sluggish diffusion effect [4], and the cocktail effect [5].

A literature review considering the past 18 years reveals that the two most widely studied high entropy alloys are the single-phase FCC CoCrFeMnNi high entropy alloys, also known as the Cantor alloy [6,7] and the single-phase BCC AlCoCrFeNiTi alloy [8]. However, it is now well accepted that focusing only on single-phase alloys usually hinders the development of both high strength and ductility. In order to overcome this strength-plasticity barrier, Lu et al. [9] developed the AlCoCrFeNi<sub>2.1</sub> eutectic high entropy alloy with a dual phase (ordered L1<sub>2</sub> FCC and B2 BCC phases), which provided both high strength and high ductility. Resulting from breaking the strength/ductility paradigm, it was hypothesized that the eutectic AlCoCrFeNi<sub>2.1</sub> alloy could replace some high temperature alloys [10] and other engineering alloys [11] used in low temperature environments.

Fusion-based welding is a key joining method where part of the material is melted, enabling the fabrication of complex-shaped structures. Fusion-based welding technologies have significant potential value for future application-oriented research and technological developments linked to the discovery of new structural materials. Therefore, assessing the weldability of these new materials is critical.

Up to now, studies on AlCoCrFeNi<sub>2.1</sub> eutectic high entropy alloys have mainly focused on their as-cast or heat treated states, studying their preparation process [6,12] and resulting properties [13,14]. The welding metallurgy and weldability of the AlCoCrFeNi<sub>2.1</sub> eutectic high entropy alloy has been studied scarcely, especially in the context of microstructure evolution and resulting mechanical properties in both the heat affected and fusion zones. Owing to the characteristics of fusion-based welding, namely the non-equilibrium solidification conditions, as well as the existence of fast heating and cooling cycles and high peak temperatures, can lead to the formation of unexpected phases or unwanted microstructural features.

Past studies that have addressed the weldability of the AlCoCrFeNi<sub>2.1</sub> eutectic high entropy alloy, primarily concentrated

on solid-state welding methods such as rotary and friction stir welding [15,16] and diffusion joining [17,18]. Moreover, only one work has focused on fusion-based welding [19]. Zhang et al. [19] used laser beam welding for joining the AlCoCrFeNi<sub>2.1</sub> eutectic high entropy alloy, obtaining good mechanical properties. Although laser welding has significant technical advantages, such as high productivity and small heat source dimensions, the high initial capital investment required for this technology can be detrimental for its implementation in industry. In contrast, gas tungsten arc welding, which is based on arc-based technology, is a low-cost alternative capable of achieving sound joints with good mechanical performance and appearance for multiple engineering alloys. Currently, the body of knowledge on the processability of the eutectic AlCoCrFeNi<sub>2.1</sub> alloy is missing the understanding of the material weldability using gas tungsten arc welding, which is a low-cost welding process for multiple industries including in the aerospace and oil & gas fields.

To bridge the aforementioned gap in literature, the as-cast AlCoCrFeNi<sub>2.1</sub> eutectic high entropy alloy was welded by gas tungsten arc welding for the first time in this work. The microstructural evolution of the welded joints was investigated using light optical microscopy, scanning electron microscopy aided by electron backscatter diffraction analysis, high energy synchrotron X-ray diffraction and thermodynamic simulations. Additionally, uniaxial tensile testing coupled with digital image correlation and micro-hardness mapping were used to evaluate the mechanical properties of the welded joints. The microstructural evolution and resulting mechanical properties were systematically evaluated, unveiling the correlation between processing, microstructure and mechanical properties.

## 2. Experimental procedures

### 2.1. Materials

Commercially pure Al, Co, Cr, Fe, Ni (99.9 wt% for Al, Co and Ni and 99.5 wt% for Cr and Fe) were used to cast the AlCoCrFeNi<sub>2.1</sub> eutectic high entropy alloy base material used in this work. Casting was performed using vacuum induction melting, with the ingot being remelted multiple times to ensure good chemical homogeneity. The dimensions of the sheets to be welded were 74 × 25 × 1.5 mm<sup>3</sup>. Before welding, the surface oxidation was removed by mechanical polishing, then ethanol and acetone were used to clean the resulting surface.

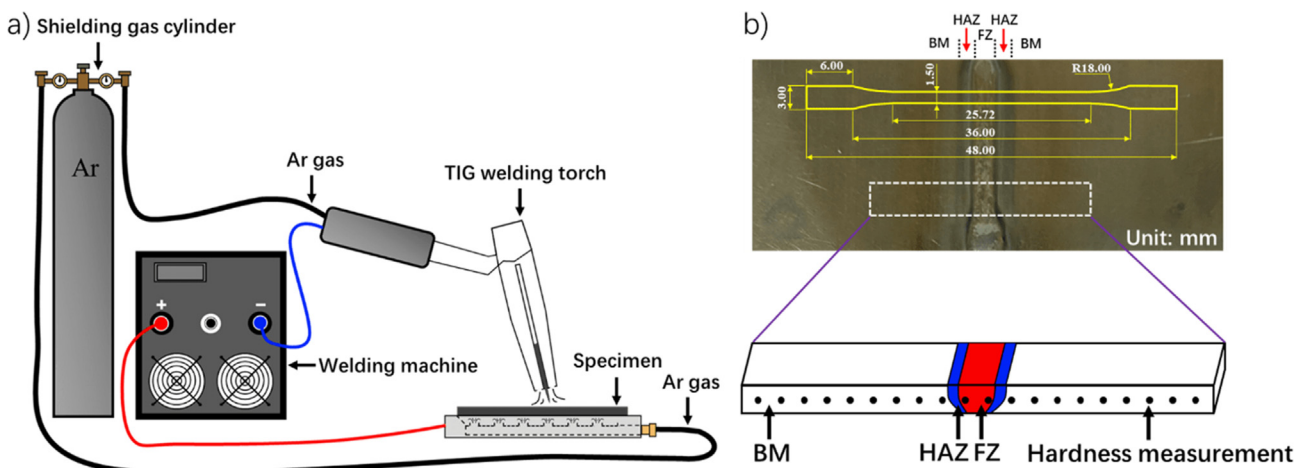


**Fig. 1.** a) Schematic representation of the experimental setup used for gas tungsten arc welding; b) Macrograph of the welded joint (face side). BM: base material; HAZ: heat affected zone; FZ: fusion zone.

## 2.2. Gas tungsten arc welding

For studying the weldability of the as-cast AlCoCrFeNi<sub>2.1</sub> eutectic high entropy alloy, gas tungsten arc welding was used. To minimize oxidation of the fusion zone and heat affected zone, 99.99 % pure Ar at a flow rate of 16 ml/min was selected as the shielding gas. The gas was injected at both the face and root of the weld to protect both sides of the joint, as schematically detailed in Fig. 1 a). Butt joints were obtained using the optimized welding parameters detailed in Table 1. To further investigate the microstructure and mechanical properties of the as-cast AlCoCrFeNi<sub>2.1</sub> eutectic high entropy alloy after welding, electrical discharge machining (EDM) was used to prepare specimens, as shown in Fig. 1 b).

## 2.3. Microstructure characterization

For microstructural characterization, the welded joint was mounted in epoxy resin and sequentially ground, polished and etched using conventional metallographic preparation techniques.

For exposing the microstructure, an etching solution composed of hydrochloric acid and nitric acid (3:1 in volume) was used for 15 s. A Leica DMI 5000 M inverted optical microscope was used for light optical microscopy. Scanning electron microscopy (SEM) and energy dispersive X-ray spectroscopy (EDS) were used for more detailed microstructural characterization using a FEI Quanta 200 environmental scanning electron microscope at the Microscopy Research Facility (MRF) at the University of North Texas (UNT), Denton, USA. In addition, electron backscatter diffraction (EBSD) was employed to study the crystallographic orientation and existing phases on a FEI Nova NanoSEM 230 with EDAX Hikari Super EBSD. TSL OIM Analysis 7.2 software was used to analyze the raw EBSD data.

High energy synchrotron X-ray diffraction was used to identify the phase structure evolution throughout the welded joint. The synchrotron experiments were performed at the P07 High Energy Materials Science beamline of PETRA III at DESY. LaB<sub>6</sub> powder was used for the calibration of the instrument parameters, and to determine the sample-to-detector (of 1226 mm). A monochro-

**Table 1**

Gas tungsten arc welding parameters for the as-cast AlCoCrFeNi<sub>2.1</sub> eutectic high entropy alloy.

Current [A]	Voltage [V]	Welding speed [mm/min]	Shielding gas	Gas flow gas [L/min]	Heat input [J/mm]
30	8	125	Argon	16	115.2

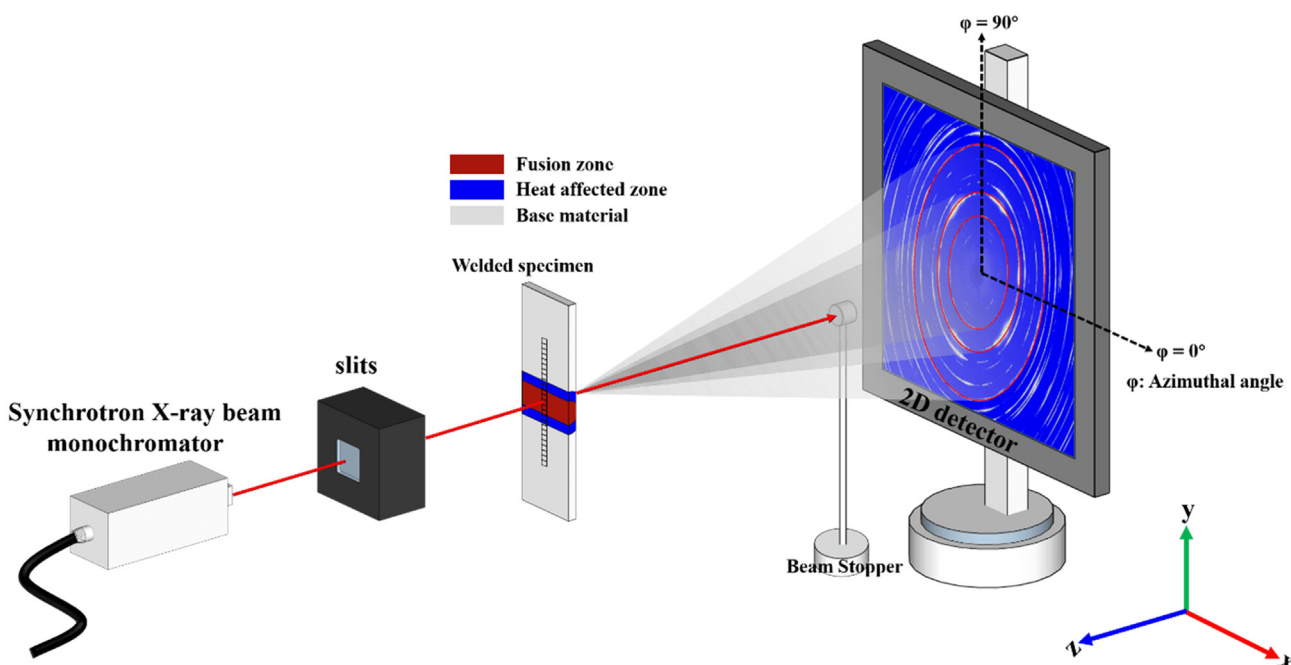


**Fig. 2.** Synchrotron X-ray diffraction setup (not to scale).

matic X-ray beam with an energy of 87 keV, corresponding to a wavelength of 0.14235 Å, was used, with a beam size of 200 μm × 200 μm. A schematic representation of the setup used is shown in Fig. 2. In transmission mode, the X-ray beam scans through the base material (BM), the heat affected zone (HAZ), the fusion zone (FZ), until it reaches the base material on the other side of the weld. The distance between consecutively analyzed spots was of 200 μm. A two-dimensional PerkinElmer fast detector was used to collect the Debye-Scherrer rings. After the acquisition of the 2D images, post-processing of the raw data was performed using Fit2D [20], HighScore Plus software [21], and the Rietveld refinement was performed using MAUD [22].

#### 2.4. Thermodynamic calculations

Thermodynamic calculations based on the CalPhiD method were used to predict how the weld thermal cycle affects the phase evolution and elemental partitioning in the fusion zone. Owing to the non-equilibrium solidification conditions experienced by the fusion zone, the Scheil-Gulliver model was used in ThermoCalc with TCHEA 5.1 HEA database. The experimental results were then compared with the predicted results for analyzing the reliability of the thermodynamic calculations, and for providing reference for further improvements on currently existing thermodynamic databases.

#### 2.5. Microhardness and mechanical testing

Microhardness mapping across the welded joints was performed on a Mitutoyo HM-112 Hardness Testing Machine with a load of 300 N, duration of 10 s, and a distance of 200 μm between consecutive indentations. Uniaxial tensile testing was performed along with digital image correlation (DIC) on a Shimadzu tensile

machine equipped with a 50 kN load cell. The dimensions of the dog-bone specimens are detailed in Fig. 1 b). Tensile tests were performed at room temperature, at a strain rate of  $1 \times 10^{-3} \text{ s}^{-1}$ , with the loading direction perpendicular to the welding direction. Before testing, the specimens were prepared for DIC by applying a random black speckle pattern over a previously painted matt white surface. Data analysis was performed using Vic-2D software. At least three specimens were used to assess the reproducibility of the tensile data after welding. After tensile testing, a Hitachi SU3800 scanning electron microscope was used to observe the fracture morphology of the welded specimens.

### 3. Results and discussion

#### 3.1. Optical and electron microscopy

Fig. 3 a) provides a cross-sectional view of the welded joint, while Fig. 3 b), c) and d) show the light optical microscopy images of the base material, heat affected zone and fusion zone, respectively. Fig. 3 e), f) and g) present detailed higher magnification electron microscopy images of the same regions. The different regions of the joints, i.e., base material, heat affected zone and fusion zone, in Fig. 3 b), c) and d), respectively, can be clearly distinguished due to differences in microstructure. From Fig. 3 a), it can be observed that the joint has full penetration without evidence of welding defects such as pores or solidification cracking.

Further observation of the microstructure of the three representative regions is detailed next starting with the base material (refer to Fig. 3 b) and e)). This region is mainly composed of ordered B2 BCC phase as well as of disordered FCC phase, as shown by the arrows marked in Fig. 3 e). The contrast in color between the white and dark phases corresponds to the FCC and B2 BCC phases, respectively, which occurs due to elemental partitioning between both

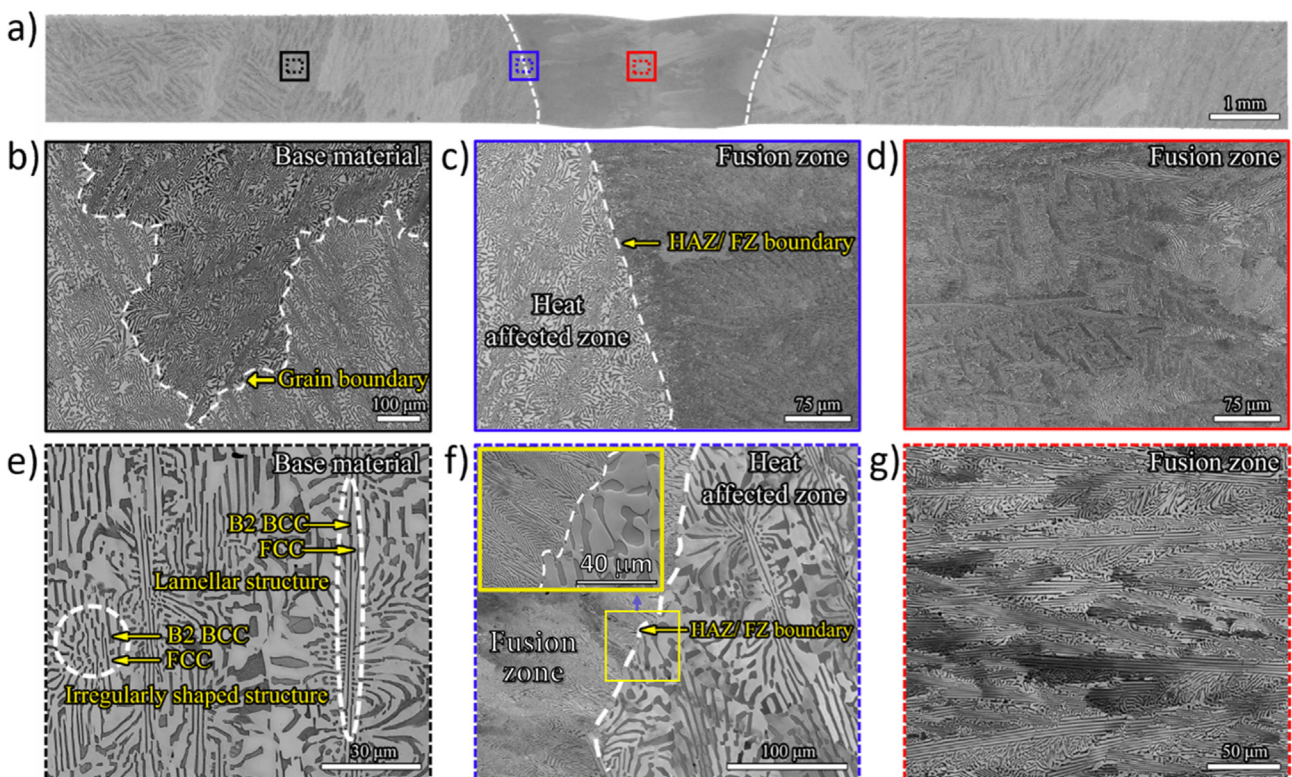


**Fig. 3.** Light optical microscopy micrographs of the as-cast AlCoCrFeNi<sub>2.1</sub> welded joint: a) overview of the weld cross-section; b) and e), c) and f), d) and g) are close-up views of the base material (BM), heat affected zone and fusion zone near the boundary (HAZ/FZ), and fusion zone (FZ), respectively.

phases as confirmed by other researchers focusing on this alloy system [23–25]. In the magnified view (refer to Fig. 3 e)), it can be observed that the base material contains both well-aligned and irregularly shaped lamellar structures.

The next region of interest corresponds to the heat affected zone (detailed in Fig. 3 c) and f), which experiences temperatures high enough to promote solid-state transformations. Compared to the initial eutectic microstructure in the base material, the FCC and B2 BCC phase structures are still observed. Moreover, the morphology of the eutectic structure remained unchanged. As documented later, changes induced at this region by the weld thermal cycle impact the nanoscale precipitates that can form in the AlCoCrFeNi<sub>2.1</sub> alloy.

The fusion zone experiences full melting, followed by a relatively fast and non-equilibrium solidification. The microstructure development in this region will largely depend on the alloy chemistry and how sensitive the material is to the off-equilibrium conditions of fusion-based welding processes [26,27]. The fusion zone microstructure is detailed in Fig. 3 d) and g), and it can be observed that the lamella thickness of the FCC and B2 BCC phases shows a significant refinement, i.e., the lamella structure becomes thinner. This difference in the lamellar thickness is related to the solidification conditions experienced during casting and welding: in casting the cooling rate is slower, which enables the development of relatively thicker lamellae, while the opposite occurs in arc-welding processes, where the higher cooling rate allows achieving a refined microstructure. The current observations coincide with the recent work of Zhang et al. using laser welding on the same alloy [19]. In addition, in the fusion zone boundary (refer to Fig. 3 c) and f)), a refined grain structure is observed owing to the faster cooling rates enabled by the colder heat affected zone that act as a substrate from where solidification progresses toward the weld centerline. This is in good agreement with the solidification theory of metals [27–29], where grain growth tends to occur in an epitaxial mode along the direction opposite to the maximum temperature gradient at the solid/liquid interface, proceeding to the center of the fusion zone and having certain preferential orientations during solidification.

A more detailed crystallographic analysis of the welded joint microstructure was performed using EBSD, as detailed in Fig. 4. Owing to the large size of the fusion zone and taking advantage of the microstructure symmetry along the weld centerline, the

EBSD map was performed only in part of the fusion zone and only on one side of the heat affected zone and base material. From Fig. 4, it can be determined that during the rapid cooling of the fusion zone, the grains of FCC and B2 BCC phases have different preferred growth directions, growing along the (101) and (001) directions, respectively. This seems inconsistent with the preferential growth along the (100) direction of cubic materials, but it is widespread in AlCoCrFeNi<sub>2.1</sub> eutectic high entropy alloys [30,31]. This can be attributed to the fact that the eutectic high entropy alloy does not cross different phase regions during cooling [9]. Further observations reveal that the fusion zone is still dominated by an eutectic lamellar structure in the welded joint (see Fig. 3 g)), indicating that the solidification rate in the fusion zone is insufficient to enable the AlCoCrFeNi<sub>2.1</sub> eutectic high entropy alloy to release itself from the eutectic growth. This is similar to the results previously reported by Zheng et al. [32] regarding the effect of different cooling rates on the solidification path of the as-cast AlCoCrFeNi<sub>2.1</sub> eutectic high entropy alloy, where different cooling rates significantly affected the solidification path. Moreover, depending on the potential composition changes in the fusion zone, the solidification microstructure may not be completely lamellar, but composed of FCC primary dendrites and of an FCC + B2 BCC eutectic structure (refer to Fig. 3 f, g) and associated insert). The former is attributed to the competitive grain growth mechanism occurring during solidification [33], while the latter is attributed to the cooling conditions experienced during welding. This aspect will be further detailed when analyzing the thermodynamic calculations.

It should be mentioned here that the above electron microscopy images did not reveal the presence of any precipitates due to limitation of resolution, although they exist, as it will be shown with the synchrotron X-ray diffraction data. In other words, the inability to detect these precipitates is related to their very low volume fraction and size. In addition to this, with EBSD it is not possible to distinguish between the disordered BCC and ordered B2 BCC phases, as they have the same crystallographic parameters. However, upon the use of high energy synchrotron X-ray diffraction both phases can be clearly distinguished, as will be detailed after.

To further elucidate the effect of welding thermal cycle on the thickness of the lamellae in the three different regions of the welded joint (base material, heat affected zone and fusion zone), Nano measurer 1.2 software was used. The average calculations are listed in Table 2.

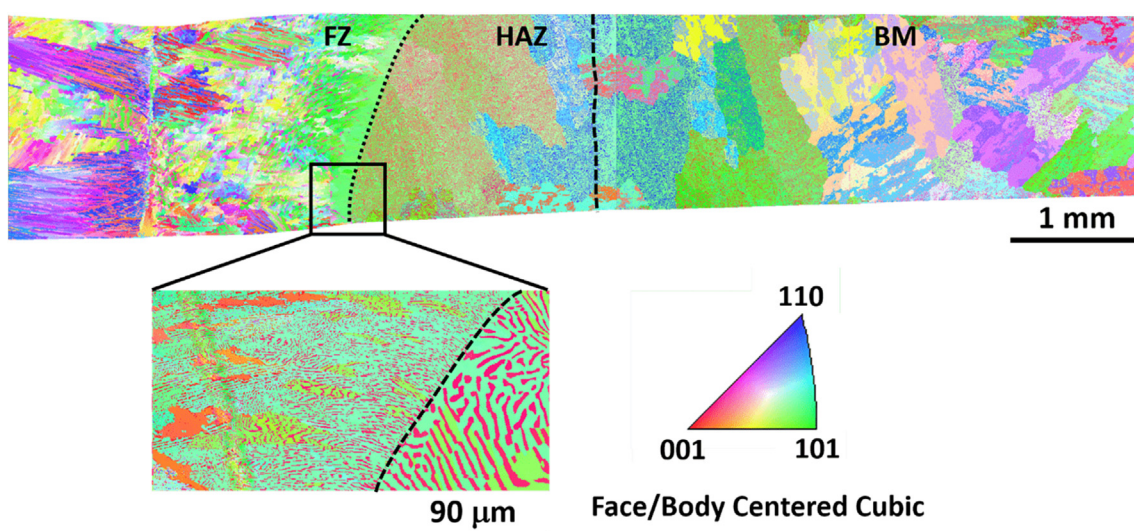


**Fig. 4.** Electron backscattered diffraction images of the AlCoCrFeNi<sub>2.1</sub> eutectic high entropy alloy welded joint.

**Table 2**

Average interlamellar thickness evolution of eutectic FCC and B2 BCC phases in the welded joint of the as-cast AlCoCrFeNi<sub>2.1</sub> eutectic high entropy alloy (BM: base material; HAZ: heat affected zone; FZ: fusion zone).

Region	Average interlamellar thickness [μm]	
	FCC phase	B2 BCC phase
BM	3.27 ± 0.44	1.66 ± 0.57
HAZ	2.85 ± 0.36	1.95 ± 0.22
FZ	0.62 ± 0.18	0.25 ± 0.07

Comparing the eutectic lamellar thickness of the base material, heat affected zone and fusion zone, significant changes can only be observed in the fusion zone against the other two regions. Wani et al. [34] found that when the as-cast AlCoCrFeNi<sub>2.1</sub> eutectic high entropy alloy was treated at different annealing temperature between 800 and 1200 °C (heat treatments that would partially correspond to the heat affected zone of the welded joint), there was no significant coarsening of the grains after annealing compared to the as-cast specimens due to slow diffusion and dual phase morphology of the eutectic high entropy alloy. Upon entering the fusion zone, the lamellar thickness of the FCC phase decreased to 0.62 ± 0.18 μm, while for the B2 BCC phase it decreased to 0.25 ± 0.07 μm. As detailed above, this refined grain

structure is attributed to the faster cooling rate in the fusion zone compared to that experienced by the cast base material [35,36].

To clarify the effect of the weld thermal cycle on the partitioning of elements in the fusion zone, EDS mapping of the constituent elements (Al, Co, Cr, Fe and Ni) was performed as shown in Fig. 5. The nominal composition of the base material, as well as the average measured composition of the base material and fusion zone are further detailed in Table 3. It should be mentioned that the EDS results show that the proportion of the elements in the base material deviates from the alloy design, especially for Al, this being attributed to its low melting point element and its partial burning during the casting process.

In the base material and heat affected zone, the FCC phase is mainly enriched in Co, Cr, and Fe, but depleted in Al and Ni. In opposition, the B2 BCC phase is mainly depleted in Co, Cr, and Fe, but abundant in Al and Ni, which is in line with previous works as detailed in [24,34]. Since among the constituent elements of the AlCoCrFeNi<sub>2.1</sub> eutectic high entropy alloy, Co, Cr, and Fe have a similar atomic radius and strong chemical compatibility, they have the tendency to form the disordered FCC phase [37], while the Al-Ni atomic pair has the largest negative mixing enthalpy, thus preferentially combining to form a Ni-Al type ordered B2 BCC phase [38]. Comparing the elemental maps obtained in both the heat affected zone and base material, it can be concluded that

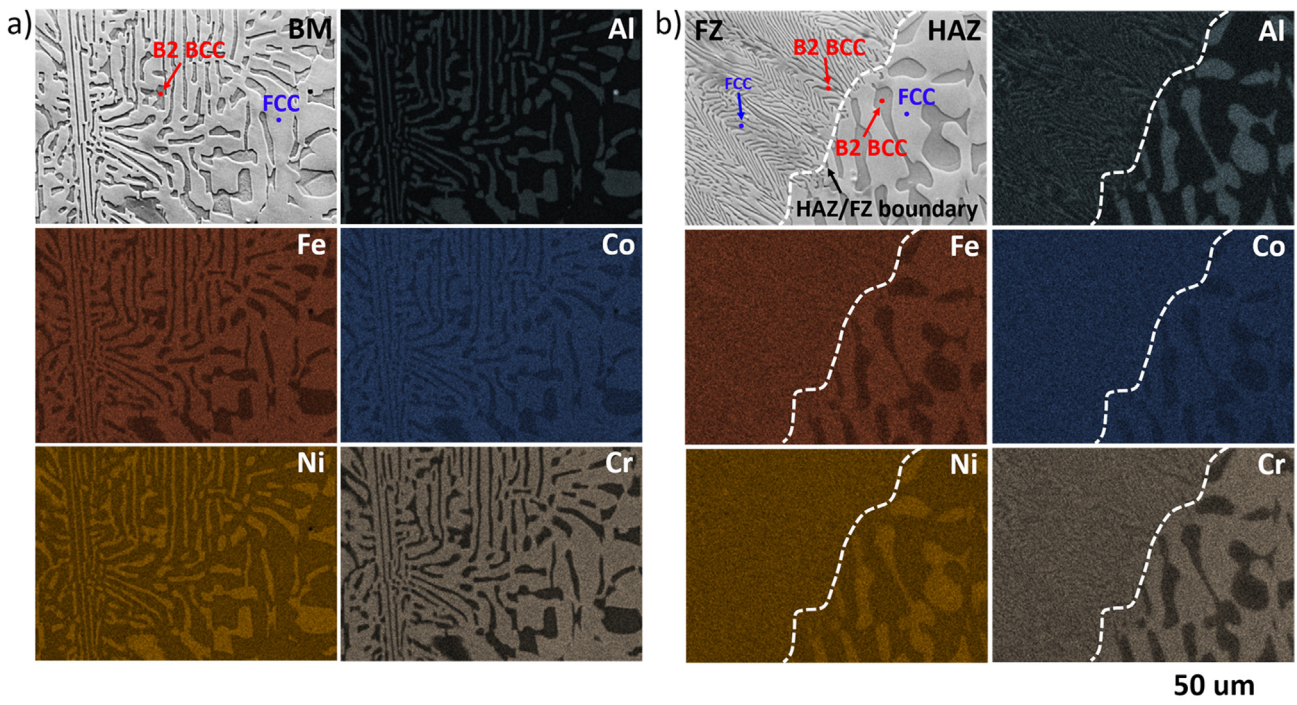


Fig. 5. EDS mapping of the as-cast AlCoCrFeNi<sub>2.1</sub> eutectic high entropy alloy joint: a) Base material; b) across the fusion zone and heat affected zone.

**Table 3**

Chemical composition of the base material and fusion zone (at.%).

Region	Elements (at.%)				
	Al	Co	Cr	Fe	Ni
Base material (Nominal)	16.39	16.39	16.39	16.39	34.44
Base material (Averaged measured)	11.18	13.02	15.72	18.19	41.89
Fusion zone (Averaged measured)	9.0	19.31	15.08	17.12	39.36

the welding peak temperature and duration in the former region is not enough to promote significant chemical differences between the major phases that exist in the material.

In the fusion zone, however, some changes exist. According to the theoretical model of Jackson and Hunt for rapid eutectic growth [39], the rapid solidification rate induced during welding can prevent the elemental partitioning and thus homogenize the material elemental composition, which is consistent with the recent work on laser welding of the same AlCoCrFeNi<sub>2.1</sub> eutectic high entropy alloy [19].

The nominal composition of the base material and that measured by EDS details key differences (refer to Table 3). It should be noted that the chemical composition given for the fusion zone is the average of multiple points taken across the fusion zone. The most significant difference concerns the loss of Al in the fusion zone, which is related to the significantly lower boiling (2519 °C), vapor pressure (100 kPa) and vaporization heat (293 kJ/mol). It should be also mentioned that preferential loss of Al due to the high temperatures experienced by the melt pool will also be location-dependent: at the joint centerline, where the temperature is the highest, an increased Al loss is expected. Resulting from this

Al loss in the fusion zone, there is some chemical redistribution of the remaining elements leading to an overall increase on the Co and Ni content in the fusion zone when compared to the as-cast base material.

### 3.2. High energy synchrotron X-ray diffraction

The microstructure of welded joints is strongly dependent on the peak temperature and cooling rate experienced by the material during welding. Moreover, the peak temperature and cooling rate varies with the distance to the center of the fusion zone [40]. To further support the above microstructure characterization, synchrotron X-ray diffraction was used to comprehensively analyze the phase structure evolution across the joint, including identification of precipitates and secondary phases. Representative individual diffraction patterns for each region are detailed in Fig. 6 a), b), c) and d), representing the base material (BM), heat affected zone near the base material (HAZ1), heat affected zone near the fusion zone (HAZ2) and fusion zone (FZ), respectively. The lattice parameters of the different phases identified across the welded joint are detailed in Table 4.

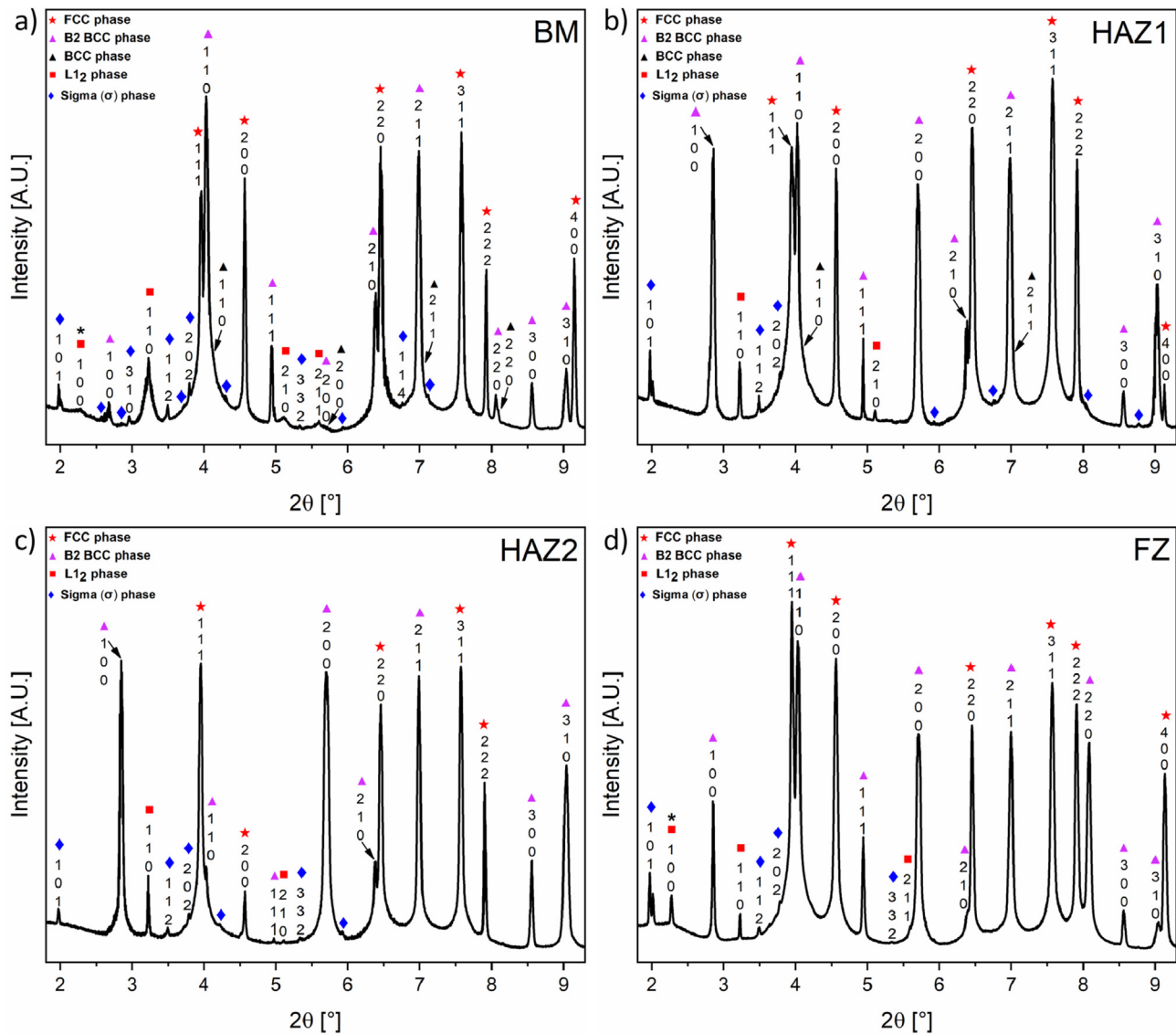


**Fig. 6.** Individual synchrotron X-ray diffraction patterns of the AlCoCrFeNi<sub>2.1</sub> eutectic high entropy alloy joint in: a) base material (BM); b) heat affected zone near the base material (HAZ1); c) heat affected zone near the fusion zone (HAZ2) and d) fusion zone (FZ).

**Table 4**

Refined lattice parameters from base material (BM), heat affected zone near the base material (HAZ1), heat affected zone near the fusion zone (HAZ2) and fusion zone (FZ) of the gas tungsten arc welded AlCoCrFeNi<sub>2.1</sub> eutectic high entropy alloy as obtained from high energy synchrotron X-ray diffraction.

Region	Phases				
	FCC	B2 BCC	BCC	L <sub>1</sub> <sub>2</sub> FCC	σ
BM	a = 3.5702 Å	a = 2.8594 Å	a = 2.8431 Å	a = 3.5574 Å	a = b = 8.1768 Å; c = 5.0185 Å; α = β = γ = 90°
HAZ1	a = 3.5705 Å	a = 2.8592 Å	a = 2.8430 Å	a = 3.5571 Å	a = b = 8.1761 Å; c = 5.0187 Å; α = β = γ = 90°
HAZ2	a = 3.5714 Å	a = 2.8587 Å	–	a = 3.5693 Å	a = b = 8.1683 Å; c = 5.1702 Å; α = β = γ = 90°
FZ	a = 3.5701 Å	a = 2.8593 Å	–	a = 3.5573 Å	a = b = 8.1771 Å; c = 5.0179 Å; α = β = γ = 90°

The phase identification from the high energy synchrotron X-ray diffraction data presented in Fig. 6 a) indicates that the base material consists of the main phases that compose the lamellar (FCC and B2 BCC phases), as well as nanosized L<sub>1</sub><sub>2</sub> FCC, disordered BCC and σ phases, as expected when the material is in the as-cast state [23].

The base material and heat affected zone close to the base material (HAZ1) possess all the same five phases: the FCC + B2 BCC phases that compose the eutectic microstructure, as well as nanoscale BCC, L<sub>1</sub><sub>2</sub> FCC and σ phases. This is in good agreement with previous transmission electron microscopy work performed by Choudhuri et al. [23], where all these phases were identified except the σ phase. Although the σ phase was not identified in [23], the DFTEM results indicate that, besides the cluster-like L<sub>1</sub><sub>2</sub> FCC nanosized phase, there still existed speckle-shaped precipitates in the L<sub>1</sub><sub>2</sub> FCC matrix phase, with Choudhuri et al. not providing a specific phase identification for these specks. In combination with the results of the synchrotron data phase identification of the present work, it can be confirmed that these diffusely distributed speckle-like precipitates can be now identified as σ phase.

When approaching the heat affected zone towards the fusion zone (HAZ2), no evidence of the BCC phase was noticed suggesting its dissolution into the material matrix owing to the higher temperatures experienced by this region during the welding process. The absence of this phase upon cooling to room temperature suggests that the cooling rate is not low enough to allow the precipitation of this phase as it occurs in the as-cast base material. The presence of this nanosized BCC phase in the as-cast AlCoCrFeNi<sub>2.1</sub> eutectic high entropy alloy is most likely due to the spinodal decomposition originating from compositional modulations in the B2 BCC phase matrix [34,41]. Wani et al. [34] found that water quenching after annealing at 800 °C was sufficient to completely dissolve the nanosized BCC phase in the B2 BCC matrix while studying the effect of aging heat treatments on the same AlCoCrFeNi<sub>2.1</sub> eutectic high entropy alloy. This is consistent with the complete dissolution of the BCC phase observed in the HAZ2 region of the welded joint in the current work.

In the fusion zone, the detected phases include the FCC and B2 BCC phases that compose the eutectic microstructure, as well as L<sub>1</sub><sub>2</sub> FCC and σ nanosized phases. The previously observed disor-

dered BCC phase is now absent, indicating that the solidification and cooling conditions experienced by this region of the joint prevented this phase to form.

It is important to mention here that the (100) superlattice reflections of the B2 BCC and L<sub>1</sub><sub>2</sub> FCC phases detected by synchrotron X-ray diffraction data provide clear evidence for the ordered structures of these FCC and BCC phases. Indeed, these results are in good agreement with previous transmission electron microscopy work, where the same superlattice reflections were observed [23]. Besides this, there are additional diffraction peaks such as (110) and (210) in the ordered FCC phase compared to those of the disordered FCC phase, as marked in Fig. 6. This is easily identified using synchrotron data, but is rarely reported in TEM characterization results.

The lattice parameters of the two matrix phases (FCC and B2 BCC) in the base material region obtained by Rietveld refinement are in good agreement with the data previously reported by Lozinko et al. [42], while the lattice constants of the nanosized phases (B2 BCC, L<sub>1</sub><sub>2</sub> FCC and σ) are detailed for the first time in this work. Comparing the evolution of the lattice parameters of the FCC and B2 BCC phases, it can be observed a decrease towards the fusion zone for the later and the opposite behavior for the former. Since no distortion of the welded joints was observed, this behavior is the way for the material to accommodate the thermal strains that occur during welding. In fact, the maximum microstrain calculated for the welded joint occurs in the heat affected zone and it takes the value of 330 με. This small microstrain can be attributed to the relatively slow cooling rate of the joint, owing to the large heat input typical of arc-based welding processes, which allows for the material to accommodate thermal strains more effectively upon cooling to room temperature.

Throughout the base material, heat affected and fusion zone the existing phases may vary. Moreover, to further quantify the changes in the volume fraction of each phase, Rietveld refinement was performed. The aim is to determine how the volume fraction of each phase varies across the welded joint. Since the thermal cycle is location dependent, the peak temperature and permanence time at temperatures that can promote solid-state transformations will vary. Table 5 summarizes the phase volume fraction of the existing phases in different regions of the welded joint as

**Table 5**

Volume fraction evolution of the FCC, B2 BCC, disordered BCC, L<sub>1</sub><sub>2</sub> FCC and σ phases across the welded joint (BM, HAZ1, HAZ2 and FZ) as obtained by Rietveld refinement and light optical micrographs.

Phases	Phase volume fraction [%]										
	FCC		B2 BCC		BCC		L <sub>1</sub> <sub>2</sub> FCC		σ		
	MAUD	ImageJ	MAUD	ImageJ	MAUD	ImageJ	MAUD	ImageJ	MAUD	ImageJ	
Region	BM	62.69	61.93	33.60	38.07	0.57	–	2.03	–	1.11	–
	HAZ1	64.40	61.46	34.08	38.54	0.19	–	0.75	–	0.58	–
	HAZ2	57.79	56.47	41.73	43.53	–	–	0.21	–	0.27	–
	FZ	86.62	84.06	12.79	15.94	–	–	0.38	–	0.21	–

determined by Rietveld refinement and by image processing using ImageJ software. Overall, there are no major deviations in the phase fraction results obtained from Rietveld refinement or by optical methods. Identification of the nanoscale phases by imaging methods was hindered by the lack of resolution of the techniques used, thus the need to complement this microstructure characterization with high energy synchrotron X-ray diffraction measurements. Synchrotron radiation as a non-destructive testing technique can then be used as a complementary characterization method alongside optical and electron microscopy which are destructive characterization tools. Moreover, with key advantages such as high photon flux and narrow beam spot sizes, it is possible to get bulk microstructure information with sufficient statistical significance for quantitative (and qualitative) characterization. A detailed analysis of the evolution of the phase volume fraction of the welded joints is presented next.

The base material primarily consists of the eutectic-composing phases with 62.69 and 33.60 % of FCC and B2 BCC phases, respectively, which is consistent with measurements made with TEM by other researchers [23,43,44]. Due to the small size and scattered distribution of the nanosized phases that may compose this material, their quantification is difficult by conventional characterization means and, so far, no quantitative analysis has been reported. However, these nanoscale phases are clearly distinguished in the low-noise diffraction data, as previously shown in Fig. 6 a). The Rietveld refinement data shows that the volume fractions of the identified nanosized L<sub>1</sub><sub>2</sub> FCC, BCC and σ phases were 2.03, 1.11 and 0.57 %, respectively.

Entering the HAZ1 region, the volume fraction of the eutectic phases does not significantly change compared to the non-affected base material. Moreover, this region still retains all the nanoscale phases identified in the base material, but there is a clear partial dissolution since the volume fractions of the L<sub>1</sub><sub>2</sub> FCC, BCC and σ phases is reduced to 0.75, 0.19 and 0.58 %, respectively. Going toward the fusion boundary but still in the heat affected zone (HAZ2), the phase volume fraction of the eutectic phases undergoes a subtle change, with the BCC phase starting to show a slight increase from 34.08 to 41.73 %, with a corresponding decrease in the volume fraction of the FCC phase from 64.40 to 57.79 %. As it will be shown in the microhardness plots, this volume fraction increase of the hard B2 BCC phase in the HAZ2 region will correspond to an increase in hardness (to be further assessed in the microhardness plots of Fig. 10). Still in HAZ2 region, the higher peak temperatures and permanence time at temperatures where solid-state transformations can occur, further promotes dissolution of the nanoscale phases, with the BCC phase dissolving into the B2 BCC matrix (refer to Fig. 6 c)).

A significant change in the volume fraction of the FCC and B2 BCC eutectic phases in the fusion zone is noted, with the volume fraction of the FCC phase increasing from 57.79 to 86.62 %, while the B2 BCC phase retained only 12.79 % after melting and rapid material solidification. However, from Fig. 6 d), it can be observed that the diffraction peaks corresponding to the B2 BCC phase possess high intensity, which is likely due to the rapid solidification in the fusion zone promoting strong texture effects in the B2 BCC phase. The nanosized L<sub>1</sub><sub>2</sub> FCC and σ phases formed in the fusion zone, although their volume fraction was slightly below than measured in the as-cast base material (0.38 and 0.21 %, respectively). Again, the fast cooling rate during welding can suppress the formation of these phases upon cooling, thus justifying the differences observed between the fusion zone and the as-cast base material.

### 3.3. CalPhiD-based calculations

The Scheil-Gulliver model was used to reproduce the solidification behavior and phase evolution of the fusion zone in the as-cast

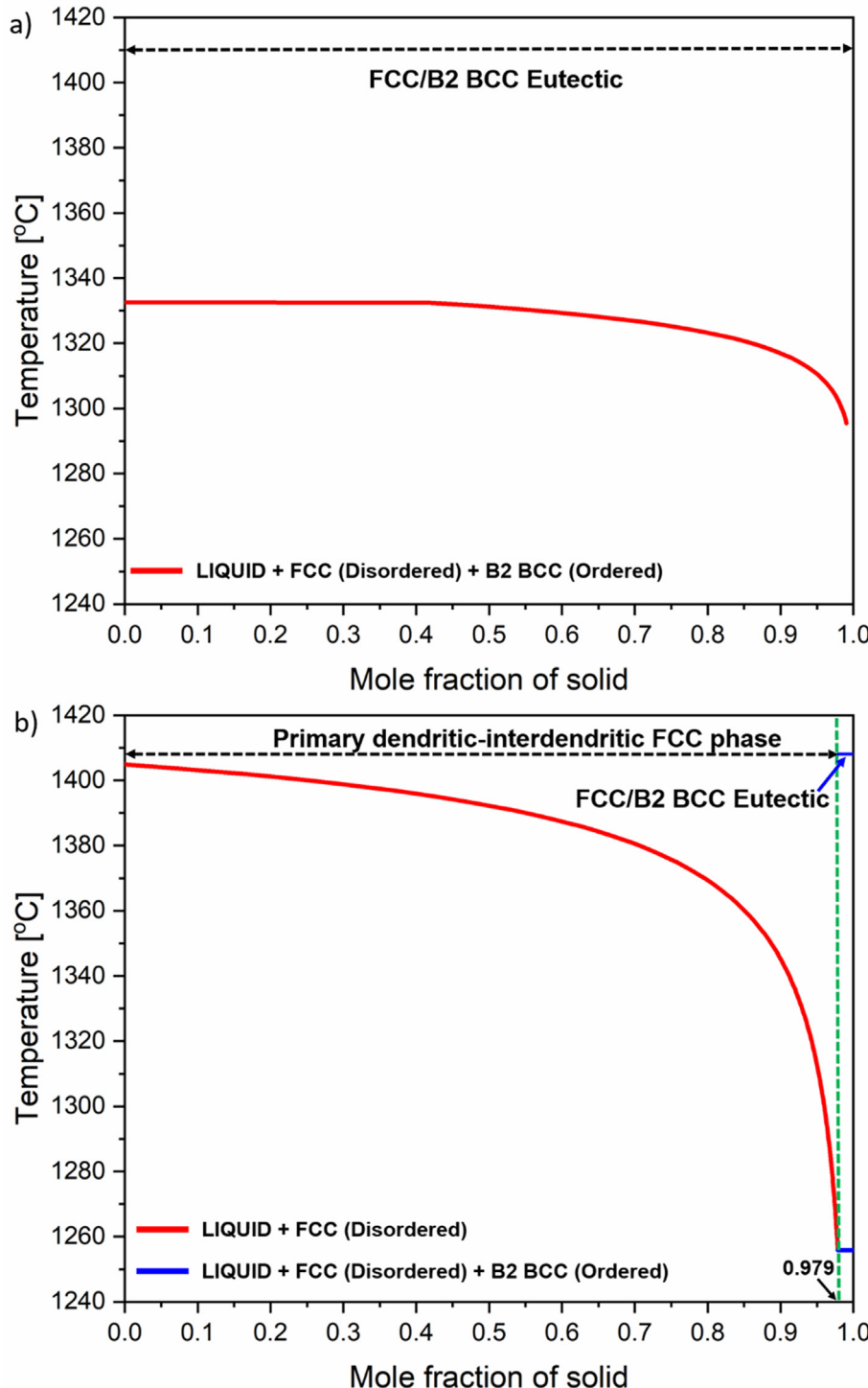
AlCoCrFeNi<sub>2.1</sub> eutectic high entropy alloy under non-equilibrium conditions. The high temperature of the melt pool induces elemental redistribution and promotes preferential loss of some elements due to evaporation, thus altering the starting nominal composition of the alloy. Therefore, to predict the solidification behavior more accurately in the fusion zone, the nominal alloy composition of the AlCoCrFeNi<sub>2.1</sub> eutectic high entropy alloy and the average elemental composition obtained by EDS measurements at multiple points in the fusion zone were used in the Scheil-Gulliver model to calculate the potential solidification pathways. It should be mentioned that the Scheil-Gulliver model simulation has three main assumptions [45]: 1) no back diffusion is considered in the solid phase; 2) diffusion in the liquid phase is extremely fast so that the liquid phase always has a homogeneous composition; and 3) phase equilibrium between liquid and solid phases is achieved at the local interface.

Fig. 7 a) details the solidification pathway from the Scheil-Gulliver model using the nominal composition of the alloy, while Fig. 7 b) considered the average fusion zone composition. From Fig. 7 a), it can be seen that the solidification pathway obtained based on the standard eutectic composition has only the eutectic reaction, which can be described as Liquid → Liquid + FCC (Disordered) + B2 BCC (Ordered) reaction. However, the solidification pathway shown in Fig. 7 b) occurs in two steps as follows: Liquid → Liquid + FCC (Disordered), and then followed by eutectic reaction of the remaining liquid, i.e., Liquid → Liquid + FCC (Disordered) + B2 BCC (Ordered).

As can be seen from the observed dendritic FCC phase in the optical micrographs of the fusion zone (refer to Fig. 3 f)), the solidification pathway of Fig. 7 b), which considered the fusion zone average composition, is more compatible with that experienced by this region of the joint. It is obvious that the elemental distribution in the fusion zone does deviates from the standard eutectic composition and can be described as a sub-eutectic fusion zone. Combined with the microstructural features of the fusion zone in Fig. 3 f), it is expected that when the composition deviates from the standard eutectic composition, solidification of the primary dendritic FCC phase from the liquid starts at a temperature of 1410 °C, followed by the eutectic reaction at 1256 °C, producing a mixed lamellar structure of disordered FCC and ordered B2 BCC phases. Compared to the nominal composition of the alloy used, the solidification pathway changes significantly. However, based both on the nominal alloy composition (Fig. 7 a)) and on the average elemental composition of the fusion zone measured by EDS (Fig. 7 b)), the eutectic microstructure predicted by thermodynamic calculations is composed of disordered FCC and ordered B2 BCC phases, which is in good agreement with the eutectic phases determined by synchrotron X-ray diffraction measurements presented above. However, the small amount of nanosized L<sub>1</sub><sub>2</sub> FCC and σ phases obtained by synchrotron X-ray diffraction in the fusion zone are not predicted by the Scheil calculations. This disagreement can be likely due to deviations in composition due to the possible presence of minor impurities in the starting materials used to cast the master alloy, thus promoting the formation of these phases.

The evolution of the elemental redistribution during non-equilibrium solidification is provided in Fig. 8. Fig. 8 a) reproduces the redistribution behavior of the elements in the dendritic and interdendritic FCC phase, as well as in the eutectic lamellar structure (FCC and B2 BCC phases). To distinguish the elemental partitioning in the FCC and B2 BCC phases among the eutectic lamellar structure, the evolution of each element in the B2 BCC phase is detailed in Fig. 8 b), so that the variation of the elemental content in the eutectic FCC phase can be deduced and compared to the dendritic FCC phase.

In Fig. 8 a), the red solid lines represent the elemental evolution in the dendrites, while the intersection between the red and blue



**Fig. 7.** Scheil-Gulliver solidification pathway calculations using ThermoCalc (TCHEA 5.1 database) considering: a) nominal alloy composition; b) average fusion zone composition.

solid lines correspond to the interdendritic composition. The blue solid lines denote the elemental partition in the FCC and B2 BCC phases of the eutectic lamellar structures. For a clearer analysis of the solidification process, the partition coefficient,  $k$ , is used to explain the chemical heterogeneity associated with solidification, being an indication of a given element to partition during solidification.  $k$  is expressed as the  $C_s/C_L$  ratio, where  $C_s$  is a given element content in the solid and  $C_L$  is the composition in the liquid. When

the partition coefficient is above 1, it reflects the enrichment of a specific element in the interdendritic region, and conversely, when the partition coefficient is below 1, it indicates an increase in the concentration of that element in the dendritic region. When  $k$  approaches 1, it represents a homogeneous distribution of that element throughout the microstructure [46]. The evolution of the red solid line in Fig. 8 a) shows that the partition coefficients for Al and Ni are larger than 1, especially for the Al, thus suggesting that the

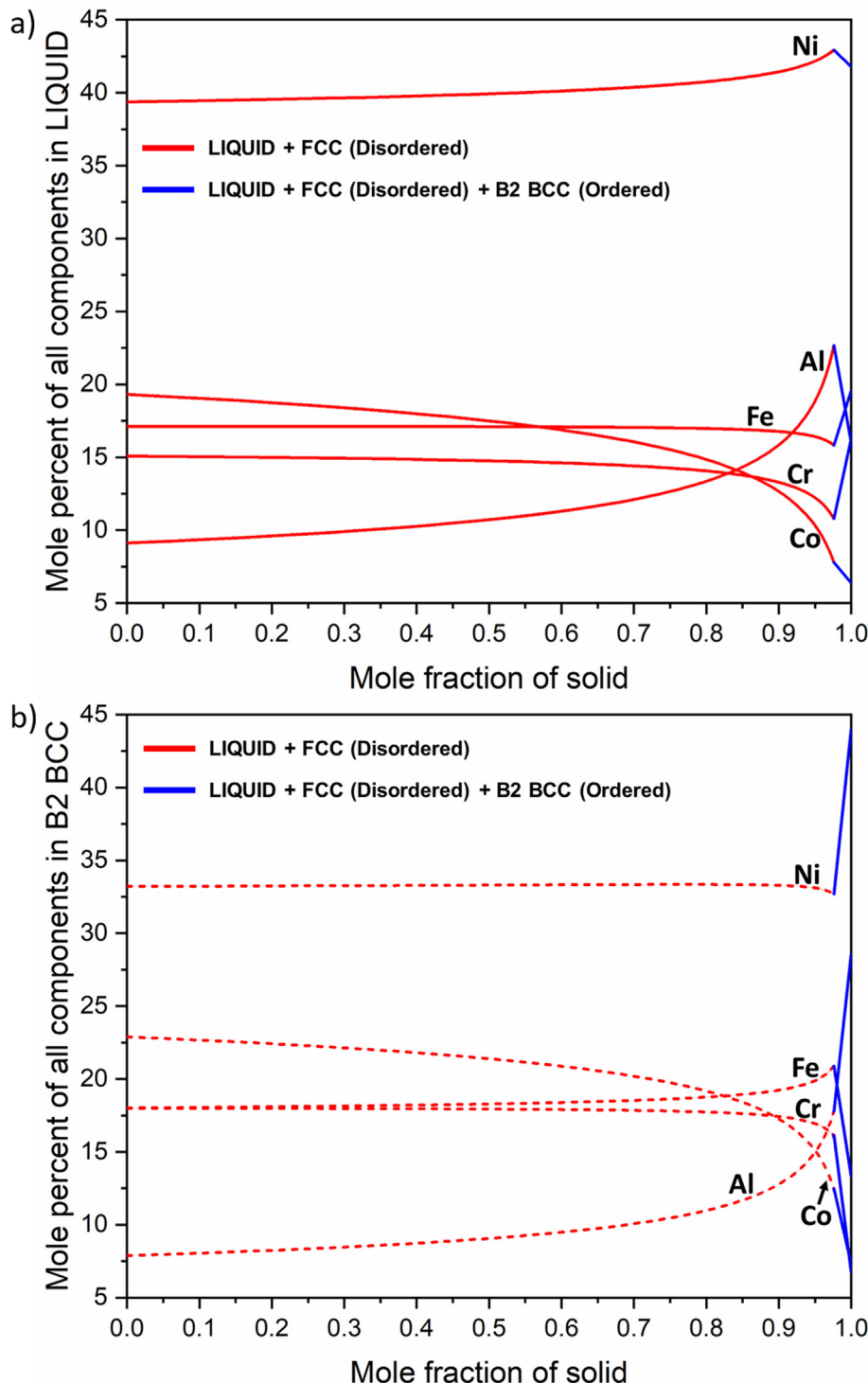


**Fig. 8.** Elemental redistribution obtained from the Scheil-Gulliver calculations for the as-cast AlCoCrFeNi<sub>2.1</sub> high entropy alloy (considering the average fusion zone composition): a) composition in the liquid phase; b) composition in the B2 BCC phase.

interdendritic region is enriched in these two elements. Especially due to the higher  $k$  of Al, the interdendritic space will be preferentially enriched in Al. Apart from this, Co, Cr and Fe all possess  $k$  values below 1, revealing that the dendritic region will be enriched in these elements. The predicted redistribution of the elements in the dendritic and interdendritic regions is consistent with that measured by EDS point scanning, as shown in Fig. 9 b) and c). A more detailed analysis and discussion of this EDS data will be given later.

The variation in the elemental composition in the B2 BCC phase is given by the blue solid line in Fig. 8 b). It can be observed that from the onset of the eutectic reaction, both Ni and Al show a linear upward trend, while the remaining elements show a downward trend, which suggests that the B2 BCC phase is enriched in Ni and Al, while the FCC phase will be enriched in Co, Cr and Fe. Combined with the evolution of the blue solid line in Fig. 8 a), it can be deduced that the eutectic FCC phase contains more Co, Cr and Fe than the B2 BCC phase.

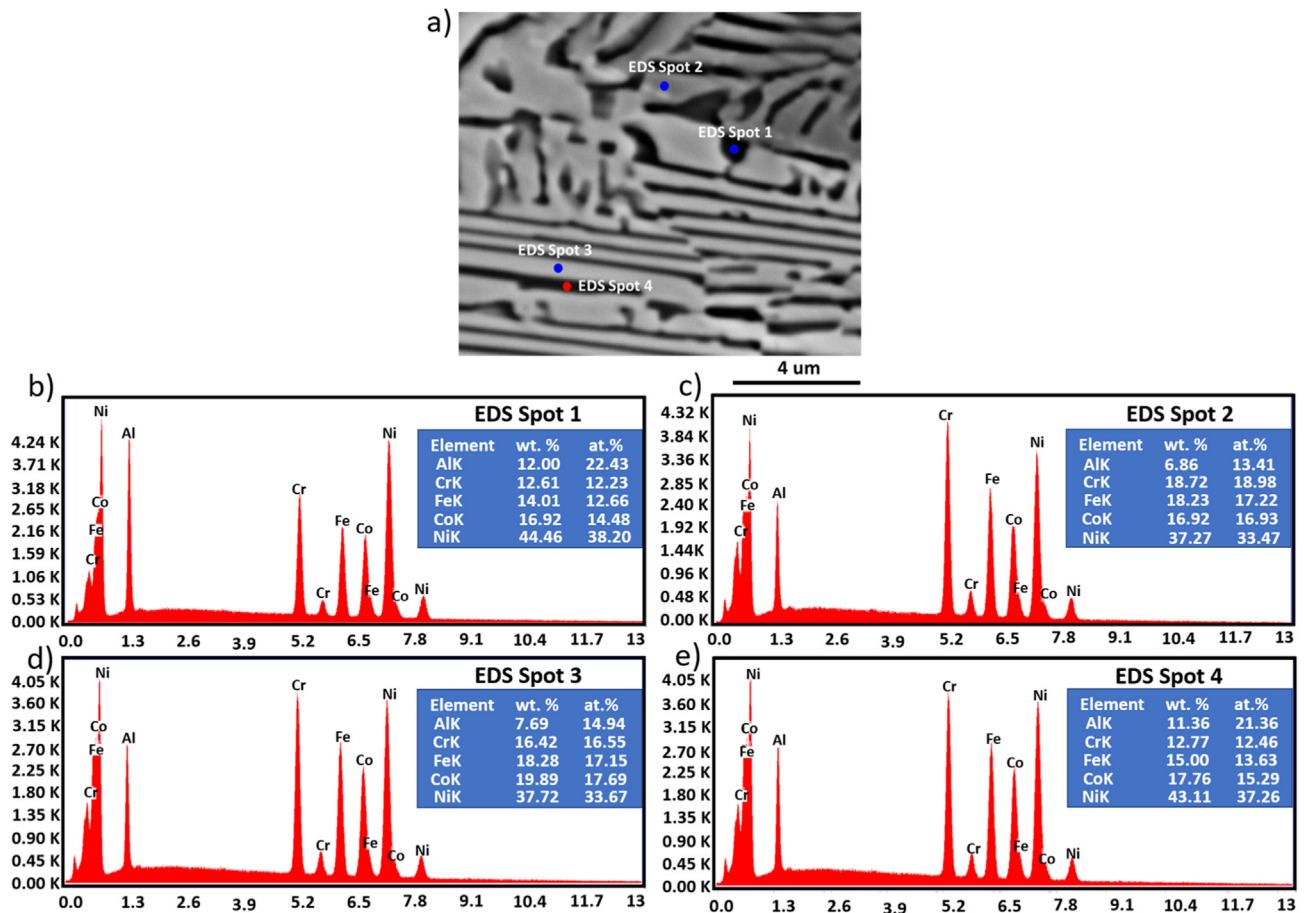


**Fig. 9.** a): Scanning electron microscopy (SEM) micrograph along with the energy-dispersive X-ray spectroscopy (EDS) point analysis in different region within the fusion zone; b to e) are EDS patterns and the resulting compositions of points 1 to 4, respectively.

To further verify the reliability of the thermodynamic calculations, Fig. 9 b), c), d) and e) detail representative point compositional results of the dendritic (spot 1) and interdendritic (spot 2) regions, the FCC phase (spot 3) and the B2 BCC phase (spot 4) in the fusion zone, respectively, to further investigate the elemental differences within these different microstructures in the fusion zone and compare them with the thermodynamic calculations.

Overall, the elemental segregation in the fusion zone is not significant, but there is still microsegregation. As can be seen from the thermodynamic calculations (refer to Fig. 8), the fusion zone first forms as FCC dendrites, followed by the eutectic FCC + B2 BCC eutectic structure. A comparison of the results from the EDS point scans in Fig. 9 b) and d) shows that, the composition of Co, Cr and Fe in the dendritic region are higher than that in the interdendritic space. Concomitantly, there is a preferential Al and Ni enrichment in the interdendritic space. The existence of these different composition domains can be attributed to microsegregation, which is commonly found in fusion-based welding processes, and depends heavily on the partition coefficient of each element in the liquid [47]. The obtained EDS measurements are consistent with the results calculated in this work using the Scheil-Gulliver model, as previously shown and discussed in Fig. 8. The occurrence of component microsegregation in dendritic structures obtained during rapid solidification was also observed in work of Güler et al. [48] for high entropy alloys of the Al-Co-Cr-Fe-Ni-Ti system. For the eutectic structure, as expected, the FCC phase in the fusion zone contains preferentially enriched in Co, Cr and Fe than in the B2 BCC phase, but the opposite occurs for Ni and Al. This observation

is, thus, in good agreement with the elemental distribution evolution calculated by the Scheil-Gulliver solidification model.

#### 3.4. Microhardness and tensile properties

For evaluating the effect of the weld thermal cycle on the local strength of the joint, microhardness mapping was performed. Fig. 10 a) details the microhardness mapping of the joint, while Fig. 10 b) details the microhardness distribution obtained at mid height of the material.

Based on the evolution of the microhardness, four distinct regions within the welded joint are identified: the base material, the heat affected zone near the base material (HAZ1), the heat affected zone near the fusion zone (HAZ2) and the fusion zone.

The base material hardness has a microhardness around 300 HV, which serves as the benchmark for comparison with the other regions of the joint. When entering in the heat affected zone (HAZ1 region), a clear downward trend to 242 HV in hardness is observed. From the previous microstructure characterization, it was observed that this region was similar to the as-cast base material. The only difference was the volume fraction of nanosized phases that existed in the FCC and B2 BCC eutectic phases (refer to Table 5). In fact, the decrease in the volume fraction of these nanosized phases can justify the decreased hardness of this region. Obviously, it is clear that the nanosized phases in the FCC and B2 BCC phases act as precipitation strengtheners, so that their (partial) dissolution will decrease the material strength. Xiong et al. [49] performed a quantitative analysis of the strengthening induced by the presence

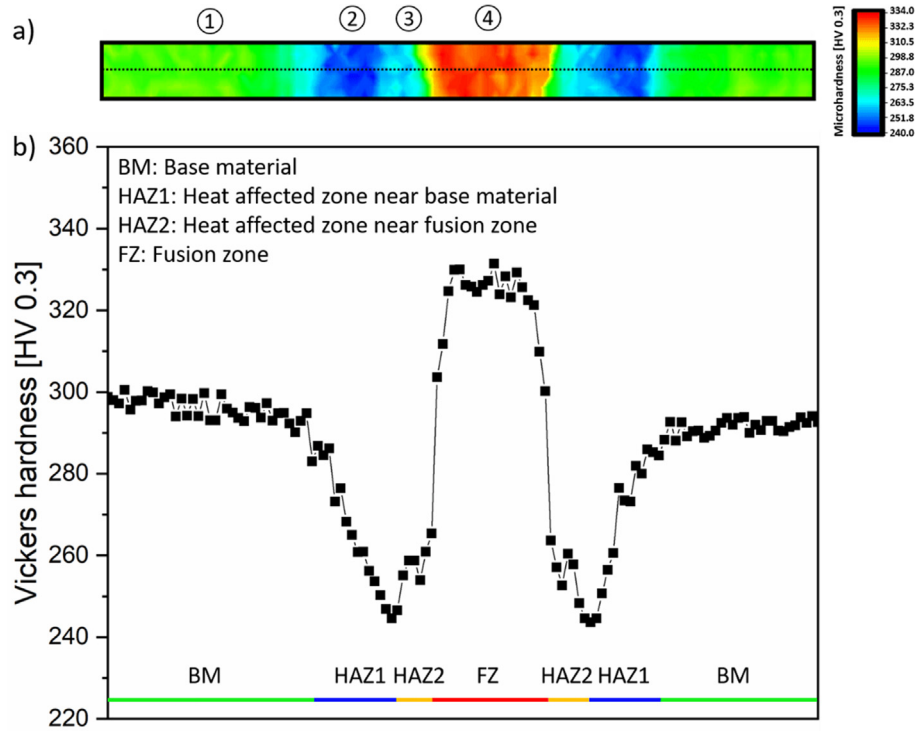


**Fig. 10.** a) Microhardness map across the welded joint; b) Microhardness profile obtained at the mid height of the welded joint (black dotted line across the hardness map in a)).

of the L1<sub>2</sub> FCC and BCC nanosized phases within the lamellar structure FCC and B2 BCC phases of the same material. Their results showed that these nanosized phases increase the alloy strengthening while sacrificing ductility. Therefore, it can be deduced that when their dissolution occurs, this will lead to a reduction in hardness, which is consistent with the results of the current paper. Still proceeding to the heat affected zone and approaching the fusion zone (HAZ2 region), there is a slight increase in hardness which is associated to the increase in the volume fraction of the hard B2 BCC phase, as previously observed from the synchrotron X-ray diffraction data.

Interestingly, the fusion zone shows a significant increase in hardness to 330 HV. This is mainly due to the considerable reduction in the lamellar thickness on this region over that observed in both the base material and heat affected zone (refer to Table 2), which is referred to as a grain refinement strengthening mechanism. The reduction in grain size increases the number of grain boundaries, which act as effective barriers to dislocation movement, thus increasing the accumulation of dislocations, supporting that grain boundary strengthening is also an auxiliary factor in this hardness increase. Miao et al. [38] previously reported that the nanosized phases and lamella thickness were the main factors influencing the microhardness of eutectic high entropy alloys. According to Miao's work, when the lamella thickness was reduced to 0.51 μm, the contribution of the phase interface was more important than that due to precipitation strengthening. Although the solidification conditions in the fusion zone resulted in a phase volume fraction of only about 10 % for the hard B2 BCC phase, as well as slightly less volume fraction of the nanosized phases, the potential hardness losses are compensated by the strengthening induced due to grain refinement.

For the purpose of assessing the effect of welding on the mechanical behavior of the as-cast AlCoCrFeNi<sub>2.1</sub> eutectic high entropy alloy, tensile experiments were also performed. Fig. 11

details representative engineering and true stress-strain curves obtained for both the base material (used as benchmark) and welded joint. The yield strength, ultimate tensile strength and elongation at fracture for each condition are detailed in Table 6.

Comparing the tensile test results obtained in both different states, it is evident that the welding process modifies the mechanical properties of the material. The yield strength increases from ≈ 284 MPa in the as-cast state to ≈ 372 MPa in the as-welded material. This increase can be explained considering the strengthening effect induced by the refined lamellar structure of the fusion zone. However, compared to the as-cast material, the plasticity in the as-welded state decreases, with the elongation being reduced from ≈ 20.6 to ≈ 13.0 %. This decrease in ductility is attributed to the composite-like structure of the welded joint, where the different mechanical behavior of the base material, heat affected zone and fusion zone, will promote a different and localized mechanical response across the joint as it will be shown with the digital image correlation data. Fracture of the welded joints systematically occurred in the non-affected base material. Further analysis of the deformation of each region of the welded joint is detailed next considering the digital image correlation data acquired. Here, it is worth mentioning that the properties of the base material used in this work are below those reported for other AlCoCrFeNi<sub>2.1</sub> eutectic high entropy alloys [50], which can be due to the raw materials used, as well as the casting conditions.

Fig. 12 was obtained considering the digital image correlation data obtained during tensile testing. Each curve corresponds to one of the three key regions of any welded joint: base material, heat affected zone and fusion zone. From Fig. 12, it can be seen that these three regions exhibit different yield strengths, which was already expected due to the microstructural changes induced by the weld thermal cycle. Considering the macroscopic elastic deformation region, it can be determined that Young's modulus, E, of each regions follows the relation E<sub>FZ</sub> > E<sub>BM</sub> > E<sub>HAZ</sub>, meaning that

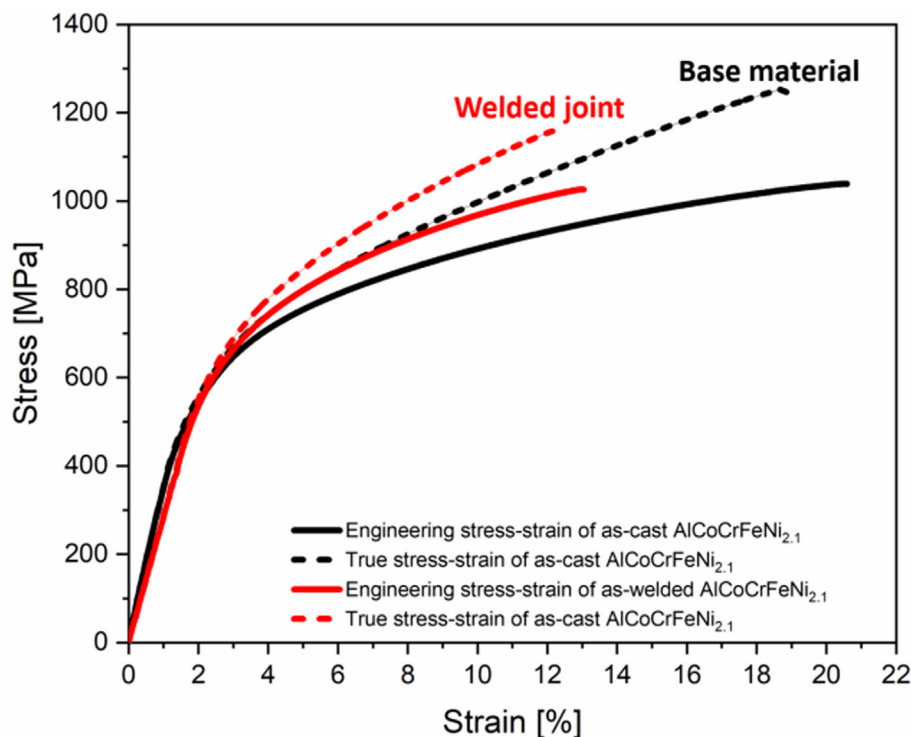


**Fig. 11.** Representative tensile stress–strain curves of base material and as-welded as-cast AlCoCrFeNi<sub>2.1</sub> eutectic high entropy alloy at room temperature under a strain rate  $10^{-3} \text{ s}^{-1}$ .

**Table 6**

Mechanical behavior of the base material and as-welded AlCoCrFeNi<sub>2.1</sub> eutectic high entropy alloy from tensile testing until failure.

Reference	Yield strength [MPa]	Ultimate tensile strength [MPa]	Fracture strain [%]
AlCoCrFeNi <sub>2.1</sub> base material	$284 \pm 8$	$1039 \pm 5$	$20.6 \pm 0.2$
Welded joint	$372 \pm 12$	$1026 \pm 10$	$13.0 \pm 0.4$

the fusion zone is the hardest, while the heat affected zone is the softest. These results are in good agreement with what would be expected solely considering the microhardness measurements previously shown in Fig. 10.

The strain in the fusion zone when failure of the joint occurred was only 7 %. The increased hardness and refined microstructure of this region will promote a preferential deformation in the softer regions of the welded joint, i.e., in the base material and heat affected zone. However, when the material fractured, the strain reached up to  $\approx 22.0$  and  $\approx 15.8$  % in the base material and heat affected zone, respectively, exhibiting a good ductility. The local deformation of the base material region is in good agreement with the bulk mechanical response of the base material specimen used to benchmark the mechanical properties against the welded joint. This also justifies why the overall joint ductility is reduced as compared to the base material specimens: the composite nature of the welded joint promotes increased strain concentration at specific regions which eventually fail.

Purely considering the local tensile curves obtained by digital image correlation of the three regions shown in Fig. 12, it would be expected that fracture would occur in the softer heat affected zone, rather than in the base material. The systematic failure of the welded joints in the base material can be related to the relatively larger volume fraction of nanosized phases which can act as stress concentrators. In the base material, there is a larger amount (relative to the heat affected zone) of dispersed and hard nanosized L<sub>1</sub><sub>2</sub> FCC, BCC [51] and  $\sigma$  phases [52], which can aid in

premature cracking development, ultimately leading to fracture in this region.

It is also possible to speculate on the load transfer behavior across the welded joint. Specifically, in the early stages of deformation, the heat affected zone, which is the softest zone, bears more of the load first, and once it yields, the load starts to be transferred to the base material. With further deformation, the initially soft heat affected zone begins to harden, allowing the initially hard base material zone to accommodate more deformation and eventually fracture due to the presence of the dispersed nanosized precipitates.

To further clarify the fracture mechanism of the welded joints, post-mortem EBSD analysis was performed. Fig. 13 a), b) and c) depict the EBSD KAM maps for the fracture area (base material region), the heat affected zone near the base material, the heat affected zone near the fusion zone and the fusion zone, respectively, while Fig. 13 d) details the KAM values distribution for these four regions. KAM maps show the local misorientation across grains, which can be used to infer on the dislocation density: the change in color from blue to red indicates an increase in the KAM values, which is associated with increased misorientation and strain distortion in the material. The comparison of the KAM maps of these four regions in the fractured specimen reveals that the KAM values increase from the fusion zone to the non-affected base material. This suggests a larger strain imparted by the base material, while the fusion zone has accommodated the least amount of plastic deformation during the tensile deforma-

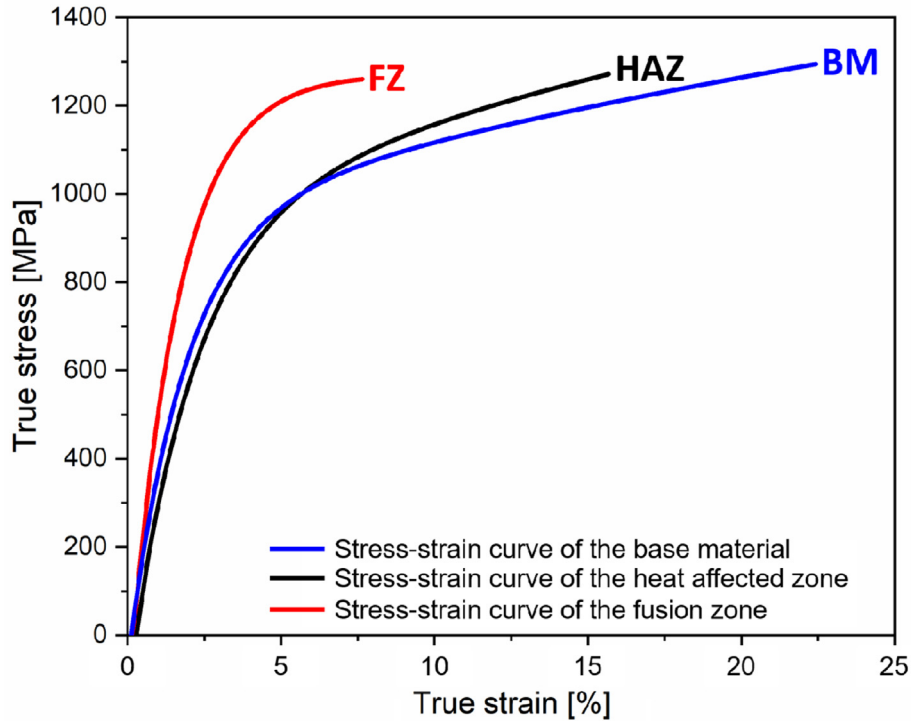


**Fig. 12.** Tensile curves obtained from the digital image correlation measurements for different regions: base material (blue line), heat affected zone (black line) and fusion zone (red line).

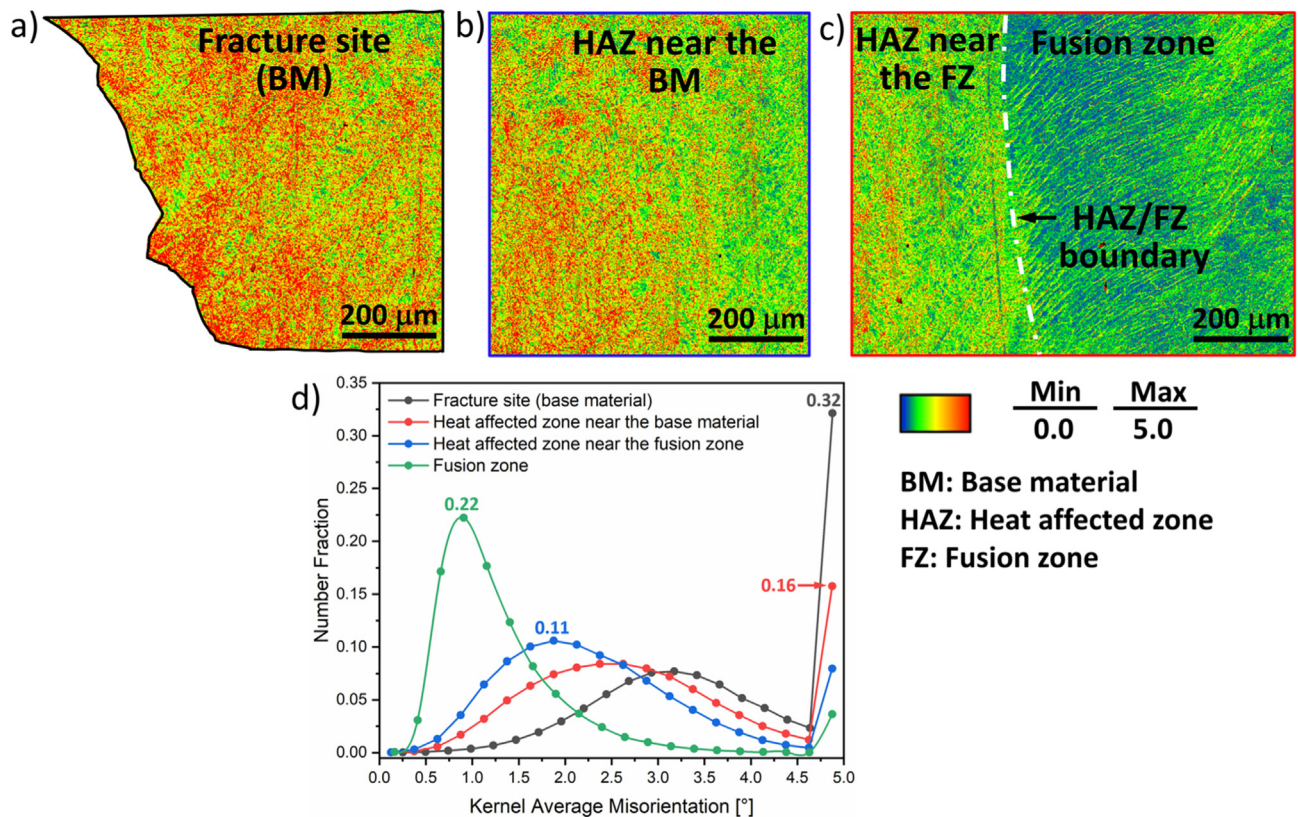


**Fig. 13.** KAM maps of the fractured specimen considering different location across the joint: a) fracture site (base material); b) heat affected zone near the base material and c) heat affected zone near the fusion zone, as well as fusion zone. d) KAM values distribution in the analyzed regions.

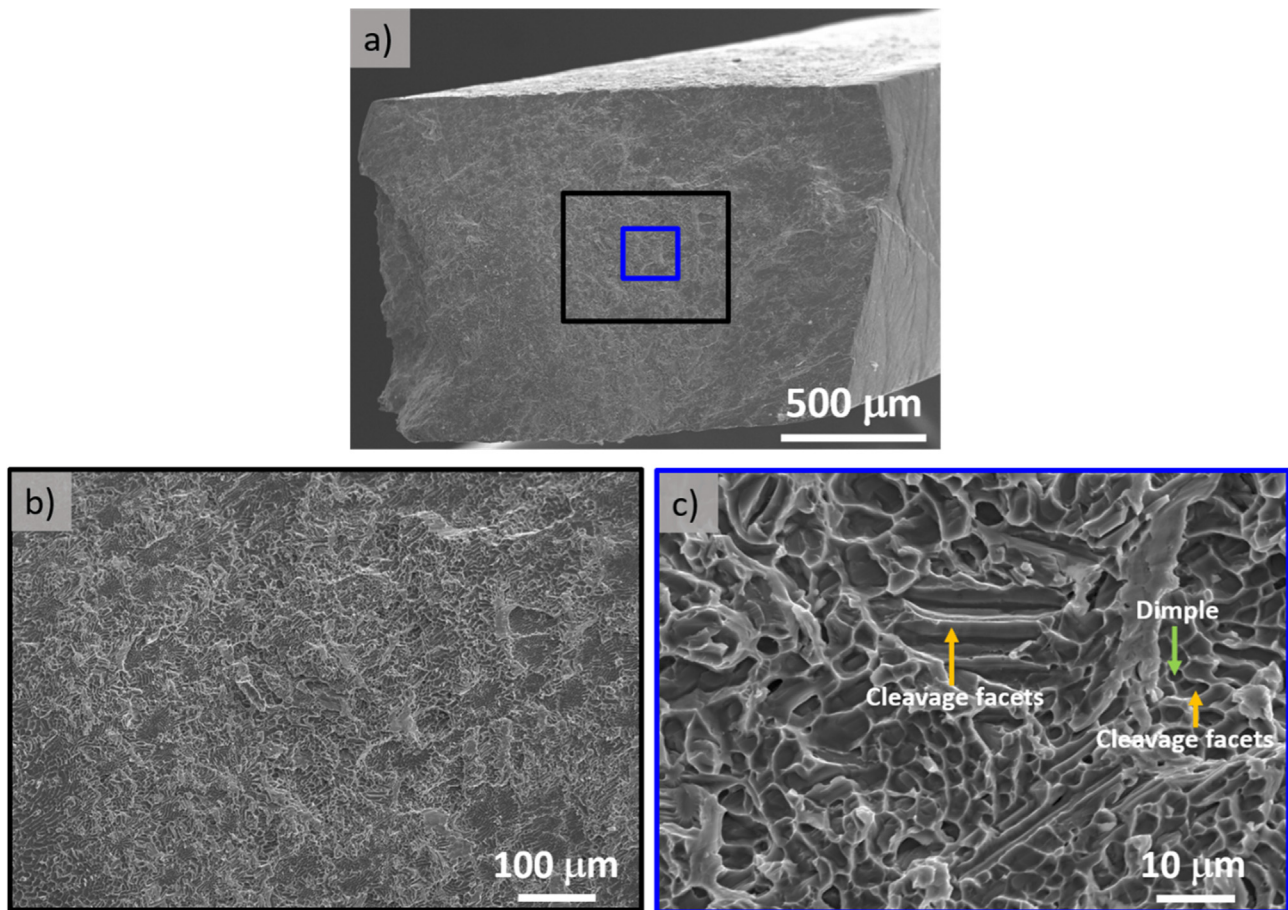


**Fig. 14.** Fracture surface analysis of the as-cast AlCoCrFeNi<sub>2.1</sub> gas tungsten arc welded joint: a) overview; b) and c) close-up detailing brittle and ductile features.

tion, owing to its refined grain structure. The associated higher dislocation density in the fractured region of the base material can be induced by the presence of preferential stress concentrator sites stress resulting from the presence of the dispersed and hard nanosized L<sub>1</sub><sub>2</sub> FCC, BCC and  $\sigma$  phases contained in the base material.

The tensile fracture morphology of the gas tungsten arc welded joints of the AlCoCrFeNi<sub>2.1</sub> eutectic high entropy alloy was observed by scanning electron microscopy, as shown in Fig. 14. As marked in Fig. 14 c), the fracture has cleavage facets, as well as a large number of ductile dimples, disclosing a mixed fracture pattern of ductility and brittleness, but with significant predominance of the former. Further observations evidence that the cleavage facets generated by the brittle B2 BCC phase coexist within the dimples of the fracture surface. It can be inferred that during the tensile loading process, the soft FCC phase is significantly deformed and gradually thinned at the upward edge, and eventually the hard B2 BCC phase remains at the bottom of the ductile dimples due to the small amount of deformation sustained by this phase. Thus, the good strength/ductility synergy of the welded joint is attributed to the joint mechanical behavior of both the soft FCC and hard B2 BCC phases.

#### 4. Conclusions

This work investigated the effect of gas tungsten arc welding on the microstructure and mechanical properties of an as-cast AlCoCrFeNi<sub>2.1</sub> eutectic high entropy alloy combining advanced

materials characterization and thermodynamic calculations. The following main conclusions can be drawn:

- (1) Gas tungsten arc welding was able to successfully produce full penetration and defect-free welded joints, suggesting the potential of this fusion-based welding process to join these advanced engineering alloys.
- (2) High energy synchrotron X-ray diffraction was used to determine the existing phases across the joint, while CalPhaD simulations were used to predict the microstructure evolution.
- (3) The weld thermal cycle did not change the eutectic structure across the whole joint, although the volume fraction of existing phases varied.
- (4) The heat affected zone evidenced softening in response to the weld thermal cycle, which is attributed to the partial dissolution of the nanosized phases that compose the starting material.
- (5) In the fusion zone, although the volume fraction of the hard B2 BCC phase is only  $\approx 12\%$ , the existence of a significantly refined microstructure renders an increased hardness compared to the as-cast base material.
- (6) Mechanical testing of the joints showed that the yield strength of the joints was higher than that of the base material, whilst there was an obvious reduction in ductility. The fracture occurred in the base material, which is mainly due to the nanosized phases contained in the base material acting as stress concentrators.

## Declaration of Competing Interest

The authors declare that they have no known competing financial interests or personal relationships that could have appeared to influence the work reported in this paper.

## Acknowledgments

JS, JGL and JPO acknowledge Fundação para a Ciência e a Tecnologia (FCT - MCTES) for its financial support via the project UID/00667/2020 (UNIDEMI). JPO acknowledges the funding by national funds from FCT - Fundação para a Ciência e a Tecnologia, I.P., in the scope of the projects LA/P/0037/2020, UID P/50025/2020 and UIDB/50025/2020 of the Associate Laboratory Institute of Nanostructures, Nanomodelling and Nanofabrication – i3N. JS acknowledges the China Scholarship Council for funding the Ph.D. grant (CSC NO. 201808320394). JGL acknowledges FCT – MCTES for funding the Ph.D. grant 2020.07350.BD. TAR acknowledges FCT – MCTES for funding the Ph.D. grant SFRH/BD/144202/2019.

The raw/processed data required to reproduce these findings cannot be shared at this time as the data also forms part of an ongoing study.

## References

- [1] J.-W. Yeh, S.-K. Chen, S.-J. Lin, J.-Y. Gan, T. Chin, T.-T. Shun, C. Tsau, S.-Y. Chang, Nanostructured High-Entropy Alloys with Multiple Principal Elements: Novel Alloy Design Concepts and Outcomes, *Adv. Eng. Mater.* 6 (2004) 299–303, <https://doi.org/10.1002/adem.200300567>.
- [2] B. Cantor, I.T.H. Chang, P. Knight, A.J.B. Vincent, Microstructural development in equiatomic multicomponent alloys, *Mater. Sci. Eng. A* 375–377 (2004) 213–218, <https://doi.org/10.1016/j.msea.2003.10.257>.
- [3] Y. Zhang, Y.J. Zhou, J.P. Lin, G.L. Chen, P.K. Liaw, Solid-Solution Phase Formation Rules for Multi-component Alloys, *Adv. Eng. Mater.* 10 (2008) 534–538, <https://doi.org/10.1002/adem.200700240>.
- [4] J. Dąbrowska, M. Zajusz, W. Kucza, G. Cieślak, K. Berent, T. Czeppe, T. Kulik, M. Danielewski, Demystifying the sluggish diffusion effect in high entropy alloys, *J. Alloys Compd.* 783 (2019) 193–207, <https://doi.org/10.1016/j.jallcom.2018.12.300>.
- [5] E.J. Pickering, N.G. Jones, High-entropy alloys: a critical assessment of their founding principles and future prospects, *Int. Mater. Rev.* 61 (2016) 183–202, <https://doi.org/10.1080/09506608.2016.1180020>.
- [6] P. Ding, A. Mao, X. Zhang, X. Jin, B. Wang, M. Liu, X. Gu, Preparation, characterization and properties of multicomponent AlCoCrFeNi2.1 powder by gas atomization method, *J. Alloys Compd.* 721 (2017) 609–614, <https://doi.org/10.1016/j.jallcom.2017.06.020>.
- [7] M.J. Yao, K.G. Pradeep, C.C. Tasan, D. Raabe, A novel, single phase, non-equiatomic FeMnNiCoCr high-entropy alloy with exceptional phase stability and tensile ductility, *Scr. Mater.* 72–73 (2014) 5–8, <https://doi.org/10.1016/j.scriptamat.2013.09.030>.
- [8] Y.J. Zhou, Y. Zhang, Y.L. Wang, G.L. Chen, Solid solution alloys of AlCoCrFeNi Ti<sub>x</sub> with excellent room-temperature mechanical properties, *Appl. Phys. Lett.* 90 (18) (2007) 181904.
- [9] Y. Lu, Y. Dong, S. Guo, L. Jiang, H. Kang, T. Wang, B. Wen, Z. Wang, J. Jie, Z. Cao, H. Ruan, T. Li, A Promising New Class of High-Temperature Alloys: Eutectic High-Entropy Alloys, *Sci. Rep.* 4 (2015) 6200, <https://doi.org/10.1038/srep06200>.
- [10] S.G. Ma, S.F. Zhang, M.C. Gao, P.K. Liaw, Y. Zhang, A Successful Synthesis of the CoCrFeNiAl0.3 Single-Crystal, High-Entropy Alloy by Bridgman Solidification, *JOM* 65 (2013) 1751–1758, <https://doi.org/10.1007/s11837-013-0733-x>.
- [11] D. Li, C. Li, T. Feng, Y. Zhang, G. Sha, J.J. Lewandowski, P.K. Liaw, Y. Zhang, High-entropy Al0.3CoCrFeNi alloy fibers with high tensile strength and ductility at ambient and cryogenic temperatures, *Acta Mater.* 123 (2017) 285–294, <https://doi.org/10.1016/j.actamat.2016.10.038>.
- [12] R. John, A. Karati, J. Joseph, D. Fabijanic, B.S. Murty, Microstructure and mechanical properties of a high entropy alloy with a eutectic composition (AlCoCrFeNi2.1) synthesized by mechanical alloying and spark plasma sintering, *J. Alloys Compd.* 835 (2020) 155424, <https://doi.org/10.1016/j.jallcom.2020.155424>.
- [13] M.H. Asoushe, A.Z. Hanzaki, H.R. Abedi, B. Mirshekari, T. Wegener, S.V. Sajadifar, T. Niendorf, Thermal stability, microstructure and texture evolution of thermomechanical processed AlCoCrFeNi2.1 eutectic high entropy alloy, *Mater. Sci. Eng. A* 799 (2021) 140012, <https://doi.org/10.1016/j.msea.2020.140012>.
- [14] Y. Dong, X. Gao, Y. Lu, T. Wang, T. Li, A multi-component AlCrFe2Ni2 alloy with excellent mechanical properties, *Mater. Lett.* 169 (2016) 62–64, <https://doi.org/10.1016/j.matlet.2016.01.096>.
- [15] P. Li, H. Sun, S. Wang, X. Hao, H. Dong, Rotary friction welding of AlCoCrFeNi2.1 eutectic high entropy alloy, *J. Alloys Compd.* 814 (2020) 152322, <https://doi.org/10.1016/j.jallcom.2019.152322>.
- [16] T. Wang, M. Komarasamy, S. Shukla, R.S. Mishra, Simultaneous enhancement of strength and ductility in an AlCoCrFeNi2.1 eutectic high-entropy alloy via friction stir processing, *J. Alloys Compd.* 766 (2018) 312–317, <https://doi.org/10.1016/j.jallcom.2018.06.337>.
- [17] P. Li, S. Wang, Y. Xia, X. Hao, H. Dong, Diffusion bonding of AlCoCrFeNi2.1 eutectic high entropy alloy to TiAl alloy, *J. Mater. Sci. Technol.* 45 (2020) 59–69, <https://doi.org/10.1016/j.jmst.2019.10.041>.
- [18] P. Li, H. Sun, S. Wang, Y. Xia, H. Dong, G. Wen, H. Zhang, Diffusion bonding of AlCoCrFeNi2.1 eutectic high entropy alloy to GH4169 superalloy, *Mater. Sci. Eng. A* 793 (2020) 139843, <https://doi.org/10.1016/j.msea.2020.139843>.
- [19] M. Zhang, D. Wang, L. He, X. Ye, W. Zhang, Laser beam welding of AlCoCrFeNi2.1 eutectic high-entropy alloy, *Mater. Lett.* 308 (2022) 131137, <https://doi.org/10.1016/j.matlet.2021.131137>.
- [20] A.P. Hammersley, FIT2D: a multi-purpose data reduction, analysis and visualization program, *J. Appl. Crystallogr.* 49 (2016) 646–652, <https://doi.org/10.1107/S160057616000455>.
- [21] T. Degen, M. Sadiki, E. Bron, U. König, G. Nébert, The HighScore suite, *Powder Diffr.* 29 (2014) S13–S18, <https://doi.org/10.1017/S0885715614000840>.
- [22] L. Lutterotti, R. Vasin, H.-R. Wenk, Rietveld texture analysis from synchrotron diffraction images. I. Calibration and basic analysis, *Powder Diffr.* 29 (2014) 76–84, <https://doi.org/10.1017/S0885715613001346>.
- [23] D. Choudhuri, S. Shukla, P.A. Jannotti, S. Muskeri, S. Mukherjee, J.T. Lloyd, R.S. Mishra, Characterization of as-cast microstructural heterogeneities and damage mechanisms in eutectic AlCoCrFeNi2.1 high entropy alloy, *Mater. Charact.* 158 (2019) 109955, <https://doi.org/10.1016/j.matchar.2019.109955>.
- [24] P. Shi, W. Ren, T. Zheng, Z. Ren, X. Hou, J. Peng, P. Hu, Y. Gao, Y. Zhong, P.K. Liaw, Enhanced strength–ductility synergy in ultrafine-grained eutectic high-entropy alloys by inheriting microstructural lamellae, *Nat. Commun.* 10 (2019) 489, <https://doi.org/10.1038/s41467-019-08460-2>.
- [25] D. Choudhuri, P.A. Jannotti, S. Muskeri, S. Shukla, S. Gangireddy, S. Mukherjee, B.E. Schuster, J.T. Lloyd, R.S. Mishra, Ballistic Response of a FCC-B2 Eutectic AlCoCrFeNi2.1 High Entropy Alloy, *J. Dyn. Behav. Mater.* 5 (2019) 495–503, <https://doi.org/10.1007/s40870-019-00220-z>.
- [26] G.J. Davies, J.G. Garland, Solidification Structures and Properties of Fusion Welds, *Int. Metall. Rev.* 20 (1975) 83–108, <https://doi.org/10.1179/imtr.1975.20.1.83>.
- [27] S.A. David, S.S. Babu, J.M. Vitek, Welding: Solidification and microstructure, *JOM* 55 (2003) 14–20, <https://doi.org/10.1007/s11837-003-0134-7>.
- [28] S.A. David, J.M. Vitek, Correlation between solidification parameters and weld microstructures, *Int. Mater. Rev.* 34 (1989) 213–245, <https://doi.org/10.1179/imr.1989.34.1.213>.
- [29] B. Gludovatz, A. Hohenwarter, D. Cattoor, E.H. Chang, E.P. George, R.O. Ritchie, A fracture-resistant high-entropy alloy for cryogenic applications, *Science* 345 (6201) (2014) 1153–1158.
- [30] T. Xiong, W. Yang, S. Zheng, Z. Liu, Y. Lu, R. Zhang, Y. Zhou, X. Shao, B. Zhang, J. Wang, F. Yin, P.K. Liaw, X. Ma, Journal of Materials Science & Technology Faceted Kurdjumov–Sachs interface-induced slip continuity in the, *J. Mater. Sci. & Technol.* 65 (2021) 216–227, <https://doi.org/10.1016/j.jmst.2020.04.073>.
- [31] Y. Zhu, S. Zhou, Z. Xiong, Y. Liang, Y. Xue, L. Wang, Enabling stronger eutectic high-entropy alloys with larger ductility by 3D printed directional lamellae, *Addit. Manuf.* 39 (2021) 101901, <https://doi.org/10.1016/j.addma.2021.101901>.
- [32] H. Zheng, R. Chen, G. Qin, X. Li, Y. Su, H. Ding, J. Guo, H. Fu, Phase separation of AlCoCrFeNi2.1 eutectic high-entropy alloy during directional solidification and their effect on tensile properties, *Intermetallics* 113 (2019) 106569, <https://doi.org/10.1016/j.intermet.2019.106569>.
- [33] C. Wang, J. Yu, Y. Zhang, Y. Yu, Phase evolution and solidification cracking sensibility in laser remelting treatment of the plasma-sprayed CrMnFeCoNi high entropy alloy coating, *Mater. Des.* 182 (2019) 108040, <https://doi.org/10.1016/j.matdes.2019.108040>.
- [34] I.S. Wani, T. Bhattacharjee, S. Sheikh, P.P. Bhattacharjee, S. Guo, N. Tsuji, Tailoring nanostructures and mechanical properties of AlCoCrFeNi2.1 eutectic high entropy alloy using thermo-mechanical processing, *Mater. Sci. Eng. A* 675 (2016) 99–109, <https://doi.org/10.1016/j.msea.2016.08.048>.
- [35] T. Nagase, M. Takemura, M. Matsumuro, T. Maruyama, Solidification Microstructure of AlCoCrFeNi<sub>2.1</sub> Eutectic High Entropy Alloy Ingots, *Mater. Trans.* 59 (2018) 255–264, <https://doi.org/10.2320/matertrans.F-M2017851>.
- [36] Q. Fan, C. Chen, C. Fan, Z. Liu, X. Cai, S. Lin, C. Yang, Effect of high Fe content on the microstructure, mechanical and corrosion properties of AlCoCrFeNi high-entropy alloy coatings prepared by gas tungsten arc cladding, *Surf. Coatings Technol.* 418 (2021) 127242, <https://doi.org/10.1016/j.surfcoat.2021.127242>.
- [37] Y.J. Liang, L. Wang, Y. Wen, B. Cheng, Q. Wu, T. Cao, Q. Xiao, Y. Xue, G. Sha, Y. Wang, Y. Ren, X. Li, L. Wang, F. Wang, H. Cai, High-content ductile coherent nanoprecipitates achieve ultrastrong high-entropy alloys, *Nat. Commun.* 9 (2018) 1–8, <https://doi.org/10.1038/s41467-018-06600-8>.
- [38] J. Miao, H. Yao, J. Wang, Y. Lu, T. Wang, T. Li, Surface modification for AlCoCrFeNi2.1 eutectic high-entropy alloy via laser remelting technology and subsequent aging heat treatment, *J. Alloys Compd.* 894 (2022) 162380, <https://doi.org/10.1016/j.jallcom.2021.162380>.
- [39] R. Trivedi, P. Magnin, W. Kurz, Theory of eutectic growth under rapid solidification conditions, *Acta Metall.* 35 (1987) 971–980, [https://doi.org/10.1016/0001-6160\(87\)90176-3](https://doi.org/10.1016/0001-6160(87)90176-3).

- [40] D. Parkes, W. Xu, D. Westerbaan, S.S. Nayak, Y. Zhou, F. Goodwin, S. Bhole, D.L. Chen, Microstructure and fatigue properties of fiber laser welded dissimilar joints between high strength low alloy and dual-phase steels, Mater. Des. 51 (2013) 665–675, <https://doi.org/10.1016/j.matdes.2013.04.076>.
- [41] C.-C. Tung, J.-W. Yeh, T. Shun, S.-K. Chen, Y.-S. Huang, H.-C. Chen, On the elemental effect of AlCoCrCuFeNi high-entropy alloy system, Mater. Lett. 61 (2007) 1–5, <https://doi.org/10.1016/j.matlet.2006.03.140>.
- [42] A. Lozinko, O. V. Mishin, T. Yu, U. Klement, S. Guo, Y. Zhang, Quantification of microstructure in a eutectic high entropy alloy AlCoCrFeNi 2.1, IOP Conf. Ser. Mater. Sci. Eng. 580 (2019) 012039. <https://doi.org/10.1088/1757-899X/580/1/012039>.
- [43] I.S. Wani, T. Bhattacharjee, S. Sheikh, I.T. Clark, M.H. Park, T. Okawa, S. Guo, P.P. Bhattacharjee, N. Tsuji, Cold-rolling and recrystallization textures of a nano-lamellar AlCoCrFeNi2.1 eutectic high entropy alloy, Intermetallics. 84 (2017) 42–51, <https://doi.org/10.1016/j.intermet.2016.12.018>.
- [44] T. Xiong, W. Yang, S. Zheng, Z. Liu, Y. Lu, R. Zhang, Y. Zhou, X. Shao, B. Zhang, J. Wang, F. Yin, P.K. Liaw, X. Ma, Faceted Kurdjumov-Sachs interface-induced slip continuity in the eutectic high-entropy alloy, AlCoCrFeNi2.1, J. Mater. Sci. Technol. 65 (2021) 216–227, <https://doi.org/10.1016/j.jmst.2020.04.073>.
- [45] D. Durinck, P.T. Jones, B. Blanpain, P. Wollants, G. Mertens, J. Elsen, Slag Solidification Modeling Using the Scheil?Gulliver Assumptions, J. Am. Ceram. Soc. 90 (2007) 1177–1185, <https://doi.org/10.1111/j.1551-2916.2007.01597.x>.
- [46] D. Piorunek, J. Frenzel, N. Jöns, C. Somsen, G. Eggeler, Chemical complexity, microstructure and martensitic transformation in high entropy shape memory alloys, Intermetallics. 122 (2020) 106792, <https://doi.org/10.1016/j.intermet.2020.106792>.
- [47] Y. Huang, M. Long, P. Liu, D. Chen, H. Chen, L. Gui, T. Liu, S. Yu, Effects of Partition Coefficients, Diffusion Coefficients, and Solidification Paths on Microsegregation in Fe-Based Multinary Alloy, Metall. Mater. Trans. B. 48 (2017) 2504–2515, <https://doi.org/10.1007/s11663-017-1045-2>.
- [48] S. Güler, E.D. Alkan, M. Alkan, Vacuum arc melted and heat treated AlCoCrFeNiTiX based high-entropy alloys: Thermodynamic and microstructural investigations, J. Alloys Compd. 903 (2022) 163901, <https://doi.org/10.1016/j.jallcom.2022.163901>.
- [49] T. Xiong, S. Zheng, J. Pang, X. Ma, High-strength and high-ductility AlCoCrFeNi2.1 eutectic high-entropy alloy achieved via precipitation strengthening in a heterogeneous structure, Scr. Mater. 186 (2020) 336–340, <https://doi.org/10.1016/j.scriptamat.2020.04.035>.
- [50] Y. Lu, X. Gao, L. Jiang, Z. Chen, T. Wang, J. Jie, H. Kang, Y. Zhang, S. Guo, H. Ruan, Y. Zhao, Z. Cao, T. Li, Directly cast bulk eutectic and near-eutectic high entropy alloys with balanced strength and ductility in a wide temperature range, Acta Mater. 124 (2017) 143–150, <https://doi.org/10.1016/j.actamat.2016.11.016>.
- [51] Y. Wang, W. Chen, J. Zhang, J. Zhou, A quantitative understanding on the mechanical behavior of AlCoCrFeNi2.1 eutectic high-entropy alloy, J. Alloys Compd. 850 (2021) 156610, <https://doi.org/10.1016/j.jallcom.2020.156610>.
- [52] S.R. Reddy, S. Yoshida, U. Sunkari, A. Lozinko, J. Joseph, R. Saha, D. Fabijanic, S. Guo, P.P. Bhattacharjee, N. Tsuji, Engineering heterogeneous microstructure by severe warm-rolling for enhancing strength-ductility synergy in eutectic high entropy alloys, Mater. Sci. Eng. A. 764 (2019) 138226, <https://doi.org/10.1016/j.msea.2019.138226>.